Title: Anti-chemokine antibodies after SARS-CoV-2 infection correlate with favorable disease course

Jonathan Muri[1]†, Valentina Cecchinato[1]†, Andrea Cavalli[1,2]*, Akanksha A. Shanbhag[1], Milos Matkovic[1], Maira Biggiogero[3], Pier Andrea Maida[3], Chiara Toscano[1], Elaheh Ghovehoud[1], Gabriela Danelon-Sargenti[1], Tao Gong[1], Pietro Piffaretti[1], Filippo Bianchini[1], Virginia Crivelli[1], Lucie Podešvová[1], Mattia Pedotti[1], David Jarrossay[1], Jacopo Sgrignani[1], Sylvia Thelen[1], Mario Uhr[4], Enos Bernasconi[5,6], Andri Rauch[7], Antonio Manzo[8], Adrian Ciurea[9], Marco B.L. Rocchi[10], Luca Varani[1], Bernhard Moser[11], Marcus Thelen[1], Christian Garzoni[12], Alessandra Franzetti-Pellanda[3], Mariagrazia Uguccioni[1,13]‡*, Davide F. Robbiani[1]‡*

Affiliations:

[1]Institute for Research in Biomedicine, Università della Svizzera italiana; Bellinzona, Switzerland.

[2]Swiss Institute of Bioinformatics; Lausanne, Switzerland.

[3]Clinical Research Unit, Clinica Luganese Moncucco; Lugano, Switzerland.

[4]Synlab Suisse; Bioggio, Switzerland.

[5]Regional Hospital Lugano, Ente Ospedaliero Cantonale; Lugano, Switzerland.

[6]Università della Svizzera italiana; Lugano, Switzerland.

[7]Department of Infectious Diseases, Inselspital, Bern University Hospital, University of Bern; Bern, Switzerland.

[8]Rheumatology and Translational Immunology Research Laboratories (LaRIT), Division of Rheumatology, IRCCS Policlinico San Matteo Foundation, University of Pavia; Pavia, Italy.

[9]Department of Rheumatology, Zurich University Hospital, University of Zurich; Zurich, Switzerland.

[10]Department of Biomolecular Sciences, Biostatistics Unit, University of Urbino; Urbino, Italy.

[11]Division of Infection & Immunity, Henry Wellcome Building, Cardiff University School of Medicine; Cardiff, United Kingdom.

[12]Internal Medicine and Infectious Diseases, Clinica Luganese Moncucco; Lugano, Switzerland.

[13]Department of Biomedical Sciences, Humanitas University; Pieve Emanuele, Italy.

*Corresponding author. Email: drobbiani@irb.usi.ch (DFR); mariagrazia.uguccioni@irb.usi.ch (MUg); andrea.cavalli@irb.usi.ch (ACa)

†These authors contributed equally to this work

‡These authors contributed equally to this work

Abstract:

Infection by SARS-CoV-2 leads to diverse symptoms, which can persist for months. While antiviral antibodies are protective, those targeting interferons and other immune factors are associated with adverse COVID-19 outcomes. Instead, we discovered that antibodies against specific chemokines are omnipresent after COVID-19, associated with favorable disease, and predictive of lack of long COVID symptoms at one year post infection. Anti-chemokine antibodies are present also in HIV-1 and autoimmune disorders, but they target different chemokines than those in COVID-19. Finally, monoclonal antibodies derived from COVID-19 convalescents that bind to the chemokine N-loop impair cell migration. Given the role of chemokines in orchestrating immune cell trafficking, naturally arising anti-chemokine antibodies associated with favorable COVID-19 may be beneficial by modulating the inflammatory response and thus bear therapeutic potential.

One-Sentence Summary:

Naturally arising anti-chemokine antibodies associate with favorable COVID-19 and are predictive of lack of long COVID.

Main Text:

The spectrum of disease manifestations upon infection with Severe acute respiratory syndrome coronavirus 2 (SARS-CoV-2) is broad (*1*). Factors that predispose people to hospitalization and death include age, gender, ethnicity, obesity, genetic predisposition, autoantibodies against

5   interferon, and comorbidities such as hypertension, diabetes, and coronary heart disease (*2-6*). Coronavirus disease 2019 (COVID-19) convalescent individuals often lament protracted symptoms over months, a condition referred to as long COVID or PASC (Post-Acute Sequelae of COVID), and are at increased risk of cardiovascular events (*7-13*). Some evidence points to a role for immune dysregulation and autoimmunity as contributors to long COVID, although

10   virus persistence has also been proposed (*14-16*). Overall, there is however little understanding of the biology underlying long COVID and of the reasons for the differences in COVID-19 manifestation.

      Chemokines are chemotactic cytokines that mediate leukocyte trafficking and activity

15   by binding to seven-transmembrane G protein-coupled receptors (*17, 18*). Chemokines play a fundamental role in health and disease, and the proper trafficking of leukocyte subsets is governed by the combinatorial diversity of their responsiveness to chemokines (*18*). In addition to elevated levels of pro-inflammatory cytokines (*e.g.* IL-6, TNF, and IL1β), higher levels of certain chemokines are observed in acute COVID-19 (*e.g.* CCL2, CCL3, CCL4,

20   CCL7, CCL8, CCL19, CXCL2, CXCL5, CXCL8, CXCL9, CXCL10, CXCL13, CXCL16 and CXCL17) and multiomic studies recently identified plasma chemokines among the most significant factors associated with COVID-19 severity (*19-25*). Accordingly, neutrophils and monocytes are recruited by chemokines to sites of infection, where they play a key role in the pathophysiology of COVID-19 by sustaining inflammation and causing tissue damage and

25   fibrosis, including in the inflammatory phase that follows virus clearance (*20, 24, 26-29*). Anti-inflammatory treatments, such as steroids and IL-6 blockade, are efficacious in hospitalized COVID-19 patients, and therapies targeting the chemokine system are under development for immunological disorders and have been proposed for COVID-19 (*18, 22, 30, 31*).

30   Similar to earlier work linking anti-cytokine antibodies to mycobacterial, staphylococcal and fungal diseases (*32-34*), autoantibodies against cytokines have been described in COVID-19. In particular, anti-type I Interferon antibodies distinguished ~10% of life-threatening pneumonia and ~20% of deaths from COVID-19 (*6, 35, 36*). Moreover,

autoantibodies characteristic of systemic autoimmune disorders, such as anti-phospholipid antibodies, anti-nuclear antibodies and rheumatoid factor, were reported in COVID-19 (*37-41*). A recent high-throughput screening by yeast display of the secretome further revealed the presence of autoantibodies against a number of immune factors, including chemokines (*42*).

5   However, anti-chemokine antibodies were infrequent by this method, and there was neither correlation with disease severity, or long COVID, nor information about the persistence of such autoantibodies over time.

We devised a peptide-based strategy to discover and measure antibodies that bind to a

10   functional region of each of the 43 human chemokines. By examining a diverse cohort, which contracted COVID-19 during 2020, we found that the presence of antibodies against specific chemokines helps to identify convalescent individuals with favorable COVID-19 disease course. Anti-chemokine monoclonal antibodies derived from these individuals block leukocyte migration and thus may be advantageous through modulation of the inflammatory response.

15

RESULTS

Anti-chemokine antibodies after COVID-19

To determine whether SARS-CoV-2 infection induces antibodies that interfere with immune cell migration, we first analyzed cells expressing the CC chemokine receptor 2 (CCR2), a key mediator of monocyte migration into the lung during infection and inflammation (*43-45*). *In vitro* chemotaxis assays were performed with three CCR2 agonists (CCL2, CCL7 and CCL8) in the presence of IgGs purified from the plasma of COVID-19 convalescent individuals or uninfected controls (n=24 and n=8, respectively; see Methods). Cell migration to CCL8 was significantly impaired (26.0% reduction; p=0.0039), suggesting the presence of blocking antibodies specific for CCL8 following COVID-19 (Fig. 1A).

Since the N-terminal loop (N-loop) of chemokines is required for receptor binding, we reasoned that biologically active antibodies would likely target this region of the chemokine (Fig. 1B) (*46*). To test this hypothesis, we synthesized a peptide comprising the N-loop of CCL8 and used it in enzyme-linked immunosorbent assays (ELISA) to analyze plasma samples obtained on average at 6 months (t=6m) after disease onset from a diverse COVID-19 cohort (Fig. 1C; tables S1 and S2). High levels of anti-CCL8 IgGs were found in two out of 71 COVID-19 convalescents, which was similar to antibodies against Interferon $\alpha2$ (IFN$\alpha2$; Fig. 1, D and E) (*6*). To examine the molecular features of anti-CCL8 antibodies, we purified memory B cells that bound to the CCL8 N-loop from the peripheral blood mononuclear cells (PBMCs) of the donor with the highest reactivity in ELISA and sequenced the antibodies (Fig. 1F; fig. S1A; see Methods). Out of 23 IgG sequences, 20 were clonally related, and 4 were cloned to produce monoclonal antibodies (aCCL8.001, aCCL8.003, aCCL8.004, aCCL8.005; table S3). All 4 antibodies similarly bound to the CCL8 N-loop (half-maximal effective concentrations EC_{50} between 11-16 ng/mL) and inhibited the migration of primary human monocytes towards CCL8 (Fig. 1, G and H; data not shown; table S4). Anti-CCL8 antibodies were specific, because they failed to bind to the most similar chemokine N-loops (fig. S1B). By the same approach, we discovered chemotaxis-blocking antibodies specific for CCL20 (fig. S1, C to E; table S4). We conclude that in COVID-19 convalescents there can be antibodies that interfere with the biologic activity of chemokines.

COVID-19 and patterns of anti-chemokine antibodies

Having validated the chemokine N-loop as target of functional antibodies, we designed peptides corresponding to the N-loop of all other human chemokines, with the goal of comprehensively examining anti-chemokine antibodies in COVID-19 (Fig. 2A; table S2).

5 Antibody levels were measured by ELISA of serial plasma dilutions and the signal plotted as heatmap (Fig. 2A; fig. S2; table S5). Analysis of all parameters by nonlinear dimensionality reduction with *t*-distributed stochastic neighbor embedding (t-SNE) revealed a clear separation between controls and COVID-19 convalescents (fig. S3A). Similar to CCL8, some convalescent plasma revealed high levels of IgGs to certain chemokines (for example CXCL13

10 and CXCL16). For these chemokines, antibody levels to the N-loop significantly correlated with those against the C-terminal region of the same chemokine, suggesting that, when present, antibodies formed against multiple chemokine epitopes (Fig. 2, A; fig. S3B). When considering antibodies against each chemokine individually, a significant difference in reactivity over uninfected control was observed for peptides corresponding to 23 of the 43 chemokines

15 (fig. S3C). Antibodies to the three chemokines with $p<10^{-4}$ (CCL19, CCL22 and CXCL17; "COVID-19 signature") clustered together, and by themselves were sufficient to correctly assign uninfected controls and COVID-19 convalescents with accuracies >95% (Fig. 2, A to C; fig. S3, C and D; see Methods). Thus, COVID-19 is associated with a specific pattern of anti-chemokine antibodies.

20 To examine the relationship between anti-chemokine antibodies and other serologic features of the COVID-19 cohort, we used ELISA and a pseudovirus-based neutralization assays to measure binding and neutralizing capacity of antibodies against SARS-CoV-2 (*47*). In agreement with previous studies, IgG binding to SARS-CoV-2 Spike receptor binding domain (RBD) and plasma half-maximal neutralizing titers (NT_{50}) against SARS-CoV-2 were

25 variable but positively correlated with each other and with age (fig. S4, A to C) (*47*). In contrast, there was no correlation between NT_{50} or anti-RBD IgGs and the levels of antibodies to the signature chemokines CCL19, CCL22 and CXCL17, or to the sum of all anti-chemokine IgG reactivities (cumulative area under the curve [AUC]; fig. S4D). A weak negative correlation between age and the sum of all anti-chemokine IgG reactivities was observed (fig.

30 S4D), but there were no differences in the levels of antibodies to the signature chemokines between males and females (fig. S4E). We conclude that, after COVID-19, antibodies against specific chemokines are not correlated with those against SARS-CoV-2.

To document the temporal evolution of anti-chemokine antibodies following COVID-19, we compared side-by-side the reactivities of plasma collected from the same cohort at approximately 6 months (t=6m) and 12 months (t=12m) from symptom onset (fig. S5A; table S1). In agreement with earlier findings (*48, 49*), antibodies to the virus RBD significantly decreased in unvaccinated COVID-19 convalescents, while they increased in those receiving at least one dose of mRNA-based COVID-19 vaccine (fig. S5B; table S1). Conversely, and regardless of vaccination status (data not shown), antibodies to the COVID-19 signature chemokine CCL19 significantly increased (2.1-fold, p<0.0001), those to CXCL17 remained generally stable, and those to CCL22 followed variable kinetics (Fig. 2D). Similar to CCL19, antibody levels to CCL8, CCL13, CCL16, CXCL7 and CX3CL1 were also augmented at 12 months, while a reduction was observed for CXCL16 (fig. S5C). To further investigate the kinetics of COVID-19 signature antibodies, we analyzed cohort individuals for which acute samples were also available (n=12; fig. S5D; table S1). During acute COVID-19, IgG antibodies to CCL19, but not to CCL22 or CXCL17, were already higher than in uninfected controls, and continued to increase until 12 months (fig. S5E). In contrast to natural infection, no significant change in antibody reactivity to any of the chemokines was observed upon COVID-19 mRNA vaccination of SARS-CoV-2 naïve individuals after about 4 months (130 days on average; n=16; fig. S5F; table S1). Therefore, unlike the antibodies to SARS-CoV-2 RBD, which decrease over time, the levels of some anti-chemokine antibodies that are present upon COVID-19 increase over one year of observation.

Autoantibodies have been detected in a portion of hospitalized COVID-19 patients, linking their presence to severe illness (*6, 38, 42*). To evaluate the relationship between the severity of acute COVID-19 and convalescent anti-chemokine IgGs, we compared individuals in our cohort who were either hospitalized because of the infection (n=50) or remained as outpatients (n=21; Fig. 2E). No significant difference in age distribution was observed between groups (age [years]: mean±SD; 60±14 in hospitalized, 57±15 in outpatients; p=0.3487), while a higher proportion of males was observed among hospitalized but not outpatients (60% and 38.1%, respectively; table S1) (*5*).

When the most significant differences in autoantibody levels were taken into account (p<10^{-4}), only the antibodies against CCL19 were higher in hospitalized individuals over uninfected controls, while antibodies against 8 chemokines (CXCL8, CCL22, CXCL16, CCL27, CXCL7, CCL20, CX3CL1, in addition to CCL19) were increased in outpatients (Fig. 2E; fig. S6A). Consistent with this finding, the outpatient but not the hospitalized individuals

displayed significantly higher cumulative anti-chemokine reactivity (p=0.0038; Fig. 2F). Thus, a broader pattern and higher overall amounts of anti-chemokine antibodies are observed at 6 months in those COVID-19 convalescents, who were outpatients during the acute phase of the disease.

Direct comparison of previously hospitalized and outpatient individuals by t-SNE analysis of all anti-chemokine datasets separated the two groups (Fig. 2G). Antibodies against three chemokines highly significantly distinguished outpatients from hospitalized subjects (p<10^{-4}): antibodies against CXCL5, CXCL8 and CCL25 were all lower in individuals with severe illness requiring hospitalization (fig. S6, A and B). The combination of antibody values against these three chemokines alone could correctly assign formerly hospitalized and outpatient individuals with an accuracy of 77.5%, which was improved to 98.6% by including anti-CCL2 antibodies ("COVID-19 hospitalization signature"; Fig. 2H; fig. S6C). Among the COVID-19 hospitalization signature antibodies, those against CCL2 positively correlated with anti-RBD IgG and NT_{50}, while those to CXCL5 and CXCL8 were negatively correlated with anti-RBD IgG and age (fig. S7A). Antibodies against CCL2 were increased in males (fig. S7B). Consistent with previous work, both anti-RBD IgG and NT_{50} values were significantly higher in hospitalized individuals compared to outpatients and in males compared to females of both groups (fig. S7C) (*47*). Thus, the anti-chemokine antibody signature that distinguishes uninfected from COVID-19 convalescents (CCL19, CCL22 and CXCL17; Fig. 2, B and C) is different from the signature associated with different severity of COVID-19 disease (CXCL5, CXCL8, CCL25 and CCL2; Fig. 2H).

Anti-chemokine antibodies and long COVID

A fraction of individuals who recover from COVID-19 experience long-term sequelae (*7-10*). To determine whether a specific pattern of anti-chemokine antibodies at t=6m is predictive of the persistence of symptoms, we collected this information from the cohort at t=12m (Fig. 3). 65.1% of all participants reported persistence of at least one symptom related to COVID-19. Among these, the average number of long-term symptoms was 3.3, and they were more frequent among formerly hospitalized individuals than outpatients (72.7% versus 47.4%; Fig. 3A; fig. S8, A and B; table S1). No differences in age, gender distribution or time from disease onset to second visit were observed between individuals with and without protracted symptoms (fig. S8C).

Convalescents with long-term sequelae showed significantly lower cumulative levels of anti-chemokine antibodies compared to those without symptoms (p=0.0135; Fig. 3B). This was particularly true for outpatients and among females (fig. S8, D and E). In contrast, anti-RBD IgG and NT_{50} values were comparable between the two groups (Fig. 3B). The total levels of anti-chemokine antibodies did not correlate with the number of symptoms (fig. S8F). These data indicate that overall higher levels of anti-chemokine antibodies at 6 months after COVID-19 are associated with absence of long-term symptoms at 12 months.

IgG antibodies against three chemokines distinguished the groups with high significance: CCL21 (p=0.0001), CXCL13 (p=0.0010) and CXCL16 (p=0.0011; Fig. 3C; fig. S8G; "Long COVID signature"). Logistic regression analysis using the antibody values for these 3 chemokines predicted the absence of persistent symptoms with 77.8% accuracy (Fig. 3D). These results indicate that specific patterns of anti-chemokine antibodies at 6 months predict the longer-term persistence of symptoms after COVID-19.

Since anti-chemokine antibodies to CXCL13 and CXCL16 are associated with favorable long COVID outcome, we next derived corresponding memory B cell antibodies from available PBMC samples (table S3; see Methods). Three N-loop binding monoclonal antibodies were obtained for CXCL16, which blocked migration of a cell line expressing the cognate receptor (CXCR6; Fig. 3, E and F; fig. S8H; tables S3 and S4). Similarly, 3 anti-CXCL13 N-loop antibodies bound in ELISA and inhibited chemotaxis of primary $CD19^+$ human B cells (Fig. 3, G and H; fig. S8I; tables S3 and S4). These data show that, like the antibodies against CCL8 and CCL20 (Fig. 1; fig. S1), antibodies that bind to the N-loop of CXCL13 and CXCL16 interfere with cell migration.

Anti-chemokine antibodies in HIV-1 and autoimmune diseases

To examine the relevance of anti-chemokine antibodies beyond COVID-19, we measured their presence in plasma from patients chronically infected with HIV-1 (n=24), and from individuals affected by Ankylosing Spondylitis (AS, n=13), Rheumatoid Arthritis (RA, n=13) and Sjögren Syndrome (SjS, n=13; Fig. 4; table S1 and S5; see Methods). While antibodies against a single chemokine distinguished COVID-19 from uninfected controls with high confidence (CCL19, $p<10^{-4}$), in HIV-1, antibodies against 14 chemokines (that did not include CCL19) were significantly increased: CCL2, CCL3, CCL4, CCL5, CCL20, CCL21, CCL22, CCL23, CCL27, CCL28, CXCL7, CXCL8, CXCL9 and CXCL12 ($p<10^{-4}$ for all; Fig. 4, A and B; fig. S9; table S5). Similarly, AS, RA and SjS shared autoantibodies against 4 chemokines: CCL4,

CCL19, CCL25 and CXCL9 ($p<10^{-4}$ for all; Fig. 4, A and B; fig. S9 and fig. S10A). Unsupervised clustering analysis with all anti-chemokine antibody values correctly categorized all COVID-19 and HIV-1 samples with 100% accuracy, while the autoimmune diseases all clustered with each other (fig. S10B; see Methods). A similar result was obtained by t-SNE analysis (Fig. 4C). Thus, patterns of anti-chemokine antibodies not only distinguish different COVID-19 trajectories, but also characterize other infections and autoimmune disorders.

5

DISCUSSION

We discovered that autoantibodies against chemokines are omnipresent after SARS-CoV-2 infection, and that higher levels of specific anti-chemokine antibodies are associated with favorable disease outcomes. Our findings contrast previous reports that connected autoantibodies to severe COVID-19 illness. For example, autoantibodies against type I interferon were detected in 10-20% of individuals with COVID-19 pneumonia or dying from COVID-19 (*6, 35*), and autoantibodies against a panel of immune molecules (including chemokines) and other self-antigens were described to occur sporadically and more frequently in critical COVID-19 (*38, 39, 42, 50*). These observations are in line with earlier work linking the presence of autoantibodies to adverse outcome in other infections (*32-34, 51, 52*).

Chemokines drive the activation and recruitment of leukocytes to sites of infection and are involved in tissue repair (*17, 18*). Accordingly, in COVID-19, several chemokines are detected in high amounts in bronchoalveolar and other fluids, fueling a pro-inflammatory environment in the lungs, which likely contributes to COVID-19 critical illness and hospitalization (*19-23*). We find the levels of autoantibodies against CXCL8, CCL25 and CXCL5 to be augmented in COVID-19 patients with milder disease over those that require hospitalization. Since these chemokines attract neutrophils and other cell types that promote inflammation and tissue remodeling, the presence of the corresponding autoantibodies suggests a protective role through dampening of the damaging inflammatory response associated with severe COVID-19. A disease-modifying role of the chemokine system in COVID-19 is further supported by transcriptomic analyses and by genetic studies identifying regions of chromosome 3 encoding for chemokine receptors to be linked to critical illness (*3, 53, 54*).

Similar to those associated with milder disease, autoantibodies to three other chemokines (CCL21, CXCL13 and CXCL16) are increased in individuals without long COVID one year after the infection. These chemokines are important for tissue trafficking and activation of T and B lymphocytes. Therefore, it is conceivable that the corresponding autoantibodies positively impact the long-term outcome of COVID-19 by antagonizing or otherwise modulating the activation, recruitment and retention of these cells during the immune response (*55*). In keeping with this observation, persistent inflammation has been proposed as a mechanism leading to the development of long COVID (*7*).

Regardless of disease trajectory, the presence of three other anti-chemokine antibodies is generally associated with COVID-19 infection: CCL19, CCL22 and CXCL17. Interestingly, IgG autoantibodies to CCL19, but not to CCL22 or CXCL17, are detected early on during the

acute phase, suggesting that they are either pre-existing or that they rapidly develop following the infection. The early detection of anti-CCL19 antibodies is consistent with the rapid upregulation of CCL19 during COVID-19 (*25*). Furthermore, we observe that antibody levels to CCL19 and to some other chemokines continue to increase between 6 and 12 months from disease onset. While dependent on the initial infection, since mRNA-based COVID-19 vaccination does not appear to induce anti-chemokine antibodies, this is unlikely to be related to chronic SARS-CoV-2 infection, because antiviral antibodies decrease during this time (*48*). Rather, the finding would be consistent with the persistence of the autoantigens within germinal centers, leading to continuous generation of antibody-secreting plasma cells (*56*).

Chemokines play an important role in HIV-1 and in autoimmune disorders (*18, 57, 58*). We find anti-chemokine antibodies also in these illnesses, but the patterns are different when compared to each other and to COVID-19. In HIV-1, a chronic viral infection, antibodies are significantly enhanced against more than half of all the chemokines, but do not include antibodies to either CCL19 or CXCL17, which are characteristic of COVID-19. Antibodies to the chemokine ligands of the HIV-1 coreceptors (CXCR4 and CCR5) are also detected at higher levels (*59*). Autoantibodies in the three autoimmune disorders are generally similar to each other, but distinct from those in infection. We speculate that these differences reflect the unique role of chemokines in each of these diseases.

Infection can trigger antibody polyreactivity and autoimmunity that are generally deleterious (*60-62*). Since here we show that post-infectious autoantibodies can be associated with positive outcomes, we favor the view of post-infectious autoantibodies as disease modifiers. In COVID-19, the infection induces the expression of chemokines, leading to a pro-inflammatory milieu that clears infected cells but also causes collateral damage (*20, 24, 26-29*). The variety and amount of anti-chemokine antibodies that are present or induced upon infection in each individual may modulate the strength and quality of the inflammatory response, which in turn would impact disease manifestation, severity and long COVID. This could in part explain the variable success of convalescent plasma treatment in COVID-19 (*63*), for which donors were selected based on virus neutralizing activity and not for the presence of autoantibodies that could modulate the inflammatory response.

We discovered and characterized the first, human-derived monoclonal antibodies against four chemokines, including anti-CXCL13 and anti-CXCL16 antibodies that are relevant for long COVID. Consistent with the 2-step model of chemokine receptor activation (*46, 64*), all the N-loop antibodies that were tested effectively reduced chemotaxis. Similar to steroids and IL-6 blockers, which are currently deployed in the clinic, we propose that agents

that target the chemokine system could impact positively on the inflammatory phase of COVID-19 and reduce the development of long COVID.

REFERENCES

1. C. Huang *et al.*, Clinical features of patients infected with 2019 novel coronavirus in Wuhan, China. *Lancet* **395**, 497-506 (2020).

2. Q. Zhang *et al.*, Inborn errors of type I IFN immunity in patients with life-threatening COVID-19. *Science* **370**, (2020).

3. E. Pairo-Castineira *et al.*, Genetic mechanisms of critical illness in COVID-19. *Nature* **591**, 92-98 (2021).

4. C.-H. G. Initiative, Mapping the human genetic architecture of COVID-19. *Nature* **600**, 472-477 (2021).

5. F. Zhou *et al.*, Clinical course and risk factors for mortality of adult inpatients with COVID-19 in Wuhan, China: a retrospective cohort study. *Lancet* **395**, 1054-1062 (2020).

6. P. Bastard *et al.*, Autoantibodies against type I IFNs in patients with life-threatening COVID-19. *Science* **370**, (2020).

7. S. Mehandru, M. Merad, Pathological sequelae of long-haul COVID. *Nat Immunol* **23**, 194-202 (2022).

8. H. E. Davis *et al.*, Characterizing long COVID in an international cohort: 7 months of symptoms and their impact. *EClinicalMedicine* **38**, 101019 (2021).

9. B. Blomberg *et al.*, Long COVID in a prospective cohort of home-isolated patients. *Nat Med* **27**, 1607-1613 (2021).

10. A. Nalbandian *et al.*, Post-acute COVID-19 syndrome. *Nat Med* **27**, 601-615 (2021).

11. Y. Xie, E. Xu, B. Bowe, Z. Al-Aly, Long-term cardiovascular outcomes of COVID-19. *Nat Med*, (2022).

12. Y. Xie, E. Xu, Z. Al-Aly, Risks of mental health outcomes in people with covid-19: cohort study. *BMJ* **376**, e068993 (2022).

13. M. Merad, C. A. Blish, F. Sallusto, A. Iwasaki, The immunology and immunopathology of COVID-19. *Science* **375**, 1122-1127 (2022).

14. C. Phetsouphanh *et al.*, Immunological dysfunction persists for 8 months following initial mild-to-moderate SARS-CoV-2 infection. *Nat Immunol* **23**, 210-216 (2022).

15. C. Cervia *et al.*, Immunoglobulin signature predicts risk of post-acute COVID-19 syndrome. *Nat Commun* **13**, 446 (2022).

16. A. D. Proal, M. B. VanElzakker, Long COVID or Post-acute Sequelae of COVID-19 (PASC): An Overview of Biological Factors That May Contribute to Persistent Symptoms. *Front Microbiol* **12**, 698169 (2021).

17. F. Bachelerie *et al.*, International Union of Basic and Clinical Pharmacology. [corrected]. LXXXIX. Update on the extended family of chemokine receptors and introducing a new nomenclature for atypical chemokine receptors. *Pharmacol Rev* **66**, 1-79 (2014).

18. K. Chen *et al.*, Chemokines in homeostasis and diseases. *Cell Mol Immunol* **15**, 324-334 (2018).

19. D. Blanco-Melo *et al.*, Imbalanced Host Response to SARS-CoV-2 Drives Development of COVID-19. *Cell* **181**, 1036-1045 e1039 (2020).

20. M. Liao *et al.*, Single-cell landscape of bronchoalveolar immune cells in patients with COVID-19. *Nat Med* **26**, 842-844 (2020).

21. S. R. Paludan, T. H. Mogensen, Innate immunological pathways in COVID-19 pathogenesis. *Sci Immunol* **7**, eabm5505 (2022).

22. B. A. Khalil, N. M. Elemam, A. A. Maghazachi, Chemokines and chemokine receptors during COVID-19 infection. *Comput Struct Biotechnol J* **19**, 976-988 (2021).
23. C. Lucas *et al.*, Longitudinal analyses reveal immunological misfiring in severe COVID-19. *Nature* **584**, 463-469 (2020).
24. COMBAT-Consortium, A blood atlas of COVID-19 defines hallmarks of disease severity and specificity. *Cell* **185**, 916-938 e958 (2022).
25. Y. Su *et al.*, Multi-Omics Resolves a Sharp Disease-State Shift between Mild and Moderate COVID-19. *Cell* **183**, 1479-1495 e1420 (2020).
26. M. Merad, J. C. Martin, Pathological inflammation in patients with COVID-19: a key role for monocytes and macrophages. *Nat Rev Immunol* **20**, 355-362 (2020).
27. A. F. Rendeiro *et al.*, The spatial landscape of lung pathology during COVID-19 progression. *Nature* **593**, 564-569 (2021).
28. D. Wendisch *et al.*, SARS-CoV-2 infection triggers profibrotic macrophage responses and lung fibrosis. *Cell* **184**, 6243-6261 e6227 (2021).
29. D. O. Griffin *et al.*, Cytokine storm of a different flavour: The different cytokine signature of SARS-CoV-2, the cause of COVID-19, from the original SARS outbreak. *J Glob Antimicrob Resist* **24**, 90-92 (2021).
30. F. Angriman *et al.*, Interleukin-6 receptor blockade in patients with COVID-19: placing clinical trials into context. *Lancet Respir Med* **9**, 655-664 (2021).
31. A. E. Proudfoot, M. Uguccioni, Modulation of Chemokine Responses: Synergy and Cooperativity. *Front Immunol* **7**, 183 (2016).
32. K. Kisand *et al.*, Chronic mucocutaneous candidiasis in APECED or thymoma patients correlates with autoimmunity to Th17-associated cytokines. *J Exp Med* **207**, 299-308 (2010).
33. A. Puel *et al.*, Recurrent staphylococcal cellulitis and subcutaneous abscesses in a child with autoantibodies against IL-6. *J Immunol* **180**, 647-654 (2008).
34. B. Kampmann *et al.*, Acquired predisposition to mycobacterial disease due to autoantibodies to IFN-gamma. *J Clin Invest* **115**, 2480-2488 (2005).
35. P. Bastard *et al.*, Autoantibodies neutralizing type I IFNs are present in ~4% of uninfected individuals over 70 years old and account for ~20% of COVID-19 deaths. *Sci Immunol* **6**, (2021).
36. J. Damoiseaux *et al.*, Autoantibodies and SARS-CoV2 infection: The spectrum from association to clinical implication: Report of the 15th Dresden Symposium on Autoantibodies. *Autoimmun Rev* **21**, 103012 (2021).
37. M. C. Woodruff *et al.*, Relaxed peripheral tolerance drives broad de novo autoreactivity in severe COVID-19. *medRxiv*, (2021).
38. S. E. Chang *et al.*, New-onset IgG autoantibodies in hospitalized patients with COVID-19. *Nat Commun* **12**, 5417 (2021).
39. Y. Zuo *et al.*, Prothrombotic autoantibodies in serum from patients hospitalized with COVID-19. *Sci Transl Med* **12**, (2020).
40. Y. Zhou *et al.*, Clinical and Autoimmune Characteristics of Severe and Critical Cases of COVID-19. *Clin Transl Sci* **13**, 1077-1086 (2020).
41. M. G. P. van der Wijst *et al.*, Type I interferon autoantibodies are associated with systemic immune alterations in patients with COVID-19. *Sci Transl Med* **13**, eabh2624 (2021).
42. E. Y. Wang *et al.*, Diverse functional autoantibodies in patients with COVID-19. *Nature* **595**, 283-288 (2021).

43. I. F. Charo *et al.*, Molecular cloning and functional expression of two monocyte chemoattractant protein 1 receptors reveals alternative splicing of the carboxyl-terminal tails. *Proc Natl Acad Sci U S A* **91**, 2752-2756 (1994).

44. M. Uguccioni, M. D'Apuzzo, M. Loetscher, B. Dewald, M. Baggiolini, Actions of the chemotactic cytokines MCP-1, MCP-2, MCP-3, RANTES, MIP-1 alpha and MIP-1 beta on human monocytes. *Eur J Immunol* **25**, 64-68 (1995).

45. C. Shi, E. G. Pamer, Monocyte recruitment during infection and inflammation. *Nat Rev Immunol* **11**, 762-774 (2011).

46. M. P. Crump *et al.*, Solution structure and basis for functional activity of stromal cell-derived factor-1; dissociation of CXCR4 activation from binding and inhibition of HIV-1. *EMBO J* **16**, 6996-7007 (1997).

47. D. F. Robbiani *et al.*, Convergent antibody responses to SARS-CoV-2 in convalescent individuals. *Nature* **584**, 437-442 (2020).

48. C. Gaebler *et al.*, Evolution of antibody immunity to SARS-CoV-2. *Nature* **591**, 639-644 (2021).

49. F. Gallais *et al.*, Evolution of antibody responses up to 13 months after SARS-CoV-2 infection and risk of reinfection. *EBioMedicine* **71**, 103561 (2021).

50. Y. Su *et al.*, Multiple early factors anticipate post-acute COVID-19 sequelae. *Cell* **185**, 881-895 e820 (2022).

51. S. K. Browne, S. M. Holland, Anticytokine autoantibodies in infectious diseases: pathogenesis and mechanisms. *Lancet Infect Dis* **10**, 875-885 (2010).

52. D. Garcia, D. Erkan, Diagnosis and Management of the Antiphospholipid Syndrome. *N Engl J Med* **378**, 2010-2021 (2018).

53. H. Zeberg, The major genetic risk factor for severe COVID-19 is associated with protection against HIV. *Proc Natl Acad Sci U S A* **119**, (2022).

54. A. Kousathanas *et al.*, Whole genome sequencing reveals host factors underlying critical Covid-19. *Nature*, (2022).

55. H. S. Howe, B. P. L. Leung, Anti-Cytokine Autoantibodies in Systemic Lupus Erythematosus. *Cells* **9**, (2019).

56. G. D. Victora, M. C. Nussenzweig, Germinal centers. *Annu Rev Immunol* **30**, 429-457 (2012).

57. R. C. Gallo, A. Garzino-Demo, A. L. DeVico, HIV infection and pathogenesis: what about chemokines? *J Clin Immunol* **19**, 293-299 (1999).

58. N. Godessart, S. L. Kunkel, Chemokines in autoimmune disease. *Curr Opin Immunol* **13**, 670-675 (2001).

59. E. A. Berger, P. M. Murphy, J. M. Farber, Chemokine receptors as HIV-1 coreceptors: roles in viral entry, tropism, and disease. *Annu Rev Immunol* **17**, 657-700 (1999).

60. H. Mouquet, M. C. Nussenzweig, Polyreactive antibodies in adaptive immune responses to viruses. *Cell Mol Life Sci* **69**, 1435-1445 (2012).

61. A. M. Ercolini, S. D. Miller, The role of infections in autoimmune disease. *Clin Exp Immunol* **155**, 1-15 (2009).

62. J. Suurmond, B. Diamond, Autoantibodies in systemic autoimmune diseases: specificity and pathogenicity. *J Clin Invest* **125**, 2194-2202 (2015).

63. A. Jorda *et al.*, Convalescent Plasma Treatment in Patients with Covid-19: A Systematic Review and Meta-Analysis. *Front Immunol* **13**, 817829 (2022).

64. I. Kufareva, C. L. Salanga, T. M. Handel, Chemokine and chemokine receptor structure and interactions: implications for therapeutic strategies. *Immunol Cell Biol* **93**, 372-383 (2015).

65.   L. R. Baden *et al.*, Efficacy and Safety of the mRNA-1273 SARS-CoV-2 Vaccine. *N Engl J Med* **384**, 403-416 (2021).

66.   F. P. Polack *et al.*, Safety and Efficacy of the BNT162b2 mRNA Covid-19 Vaccine. *N Engl J Med* **383**, 2603-2615 (2020).

67.   V. Cecchinato *et al.*, Impairment of CCR6+ and CXCR3+ Th Cell Migration in HIV-1 Infection Is Rescued by Modulating Actin Polymerization. *J Immunol* **198**, 184-195 (2017).

68.   I. Bello-Rivero *et al.*, Characterization of the immunoreactivity of anti-interferon alpha antibodies in myasthenia gravis patients. Epitope mapping. *J Autoimmun* **23**, 63-73 (2004).

69.   E. Shrock *et al.*, Viral epitope profiling of COVID-19 patients reveals cross-reactivity and correlates of severity. *Science* **370**, (2020).

70.   I. Clark-Lewis, L. Vo, P. Owen, J. Anderson, Chemical synthesis, purification, and folding of C-X-C and C-C chemokines. *Methods Enzymol* **287**, 233-250 (1997).

71.   B. Moepps, M. Thelen, Monitoring Scavenging Activity of Chemokine Receptors. *Methods Enzymol* **570**, 87-118 (2016).

72.   R. De Gasparo *et al.*, Bispecific IgG neutralizes SARS-CoV-2 variants and prevents escape in mice. *Nature* **593**, 424-428 (2021).

73.   P. Ogilvie, G. Bardi, I. Clark-Lewis, M. Baggiolini, M. Uguccioni, Eotaxin is a natural antagonist for CCR2 and an agonist for CCR5. *Blood* **97**, 1920-1924 (2001).

74.   M. Loetscher *et al.*, TYMSTR, a putative chemokine receptor selectively expressed in activated T cells, exhibits HIV-1 coreceptor function. *Curr Biol* **7**, 652-660 (1997).

75.   D. F. Robbiani *et al.*, Recurrent Potent Human Neutralizing Antibodies to Zika Virus in Brazil and Mexico. *Cell* **169**, 597-609 e511 (2017).

76.   T. Tiller *et al.*, Efficient generation of monoclonal antibodies from single human B cells by single cell RT-PCR and expression vector cloning. *J Immunol Methods* **329**, 112-124 (2008).

77.   L. von Boehmer *et al.*, Sequencing and cloning of antigen-specific antibodies from mouse memory B cells. *Nat Protoc* **11**, 1908-1923 (2016).

78.   J. Ye, N. Ma, T. L. Madden, J. M. Ostell, IgBLAST: an immunoglobulin variable domain sequence analysis tool. *Nucleic Acids Res* **41**, W34-40 (2013).

79.   N. T. Gupta *et al.*, Change-O: a toolkit for analyzing large-scale B cell immunoglobulin repertoire sequencing data. *Bioinformatics* **31**, 3356-3358 (2015).

80.   F. Schmidt *et al.*, Measuring SARS-CoV-2 neutralizing antibody activity using pseudotyped and chimeric viruses. *J Exp Med* **217**, (2020).

81.   Y. Zheng *et al.*, Structure of CC chemokine receptor 2 with orthosteric and allosteric antagonists. *Nature* **540**, 458-461 (2016).

82.   M. M. Shaik *et al.*, Structural basis of coreceptor recognition by HIV-1 envelope spike. *Nature* **565**, 318-323 (2019).

83.   D. J. Wasilko *et al.*, Structural basis for chemokine receptor CCR6 activation by the endogenous protein ligand CCL20. *Nat Commun* **11**, 3031 (2020).

84.   A. Waterhouse *et al.*, SWISS-MODEL: homology modelling of protein structures and complexes. *Nucleic Acids Res* **46**, W296-W303 (2018).

85.   J. Blaszczyk *et al.*, Complete crystal structure of monocyte chemotactic protein-2, a CC chemokine that interacts with multiple receptors. *Biochemistry* **39**, 14075-14081 (2000).

Author contributions:

Conceptualization: JM, VCe, ACa, MUg, DFR

Software: MM, JS, ACa

Validation: JM, VCe, ACa

Formal Analysis: JM, VCe, ACa, MBLR

Investigation: JM, VCe, AAS, EG, TG, FB

Resources: JM, TG, PP, FB, VCr, LP, CT, GD-S, BM, MT, DJ, ST, MP, LV, MB, PAM, AF-P, CG, MUh, EB, AR, ACi, AM

Writing – Original Draft: JM, VCe, MUg, DFR

Supervision: DFR, MUg

5   Funding Acquisition: DFR, MUg, ACa, LV, AR, EB

Competing interests: The Institute for Research in Biomedicine has filed a provisional patent application in connection with this work on which JM, VCe, ACa, MUg and DFR are inventors.

10

Data and materials availability: All data are available in the main text or the supplementary materials. Computer code for antibody sequence, logistic regression, clustering and t-SNE analyses will be deposited at GitHub upon publication

15   (https://github.com). Materials will be made available upon MTA.

Supplementary Materials

Materials and Methods

Figs. S1 to S10

20   Tables S1 to S5
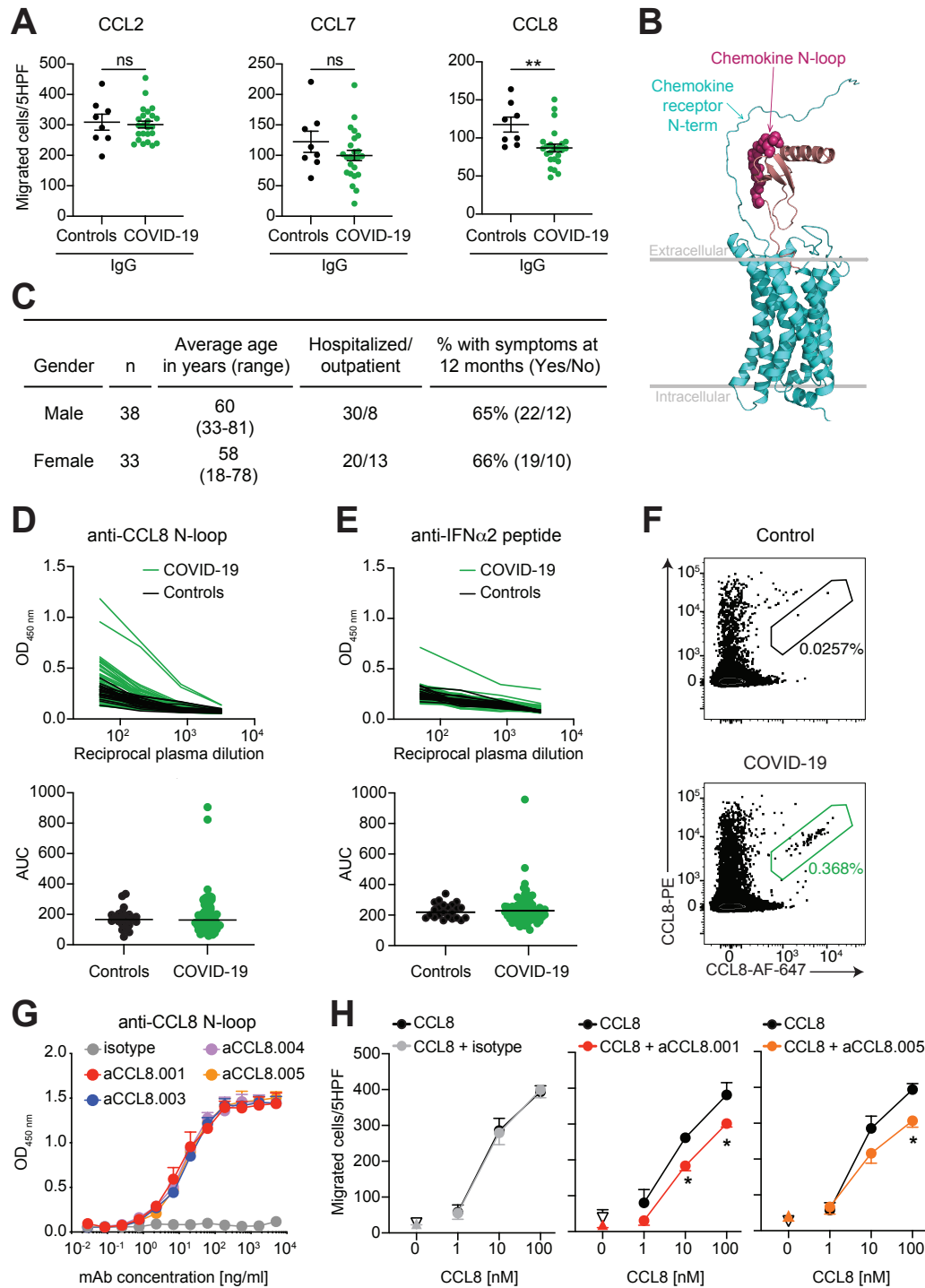
References (*65-85*)

Figure 1

Fig 1. Human monoclonal antibodies that impede CCL8 chemotaxis. (**A**) IgGs from COVID-19 convalescents inhibit CCL8 chemotaxis. Chemotaxis of CCR2 expressing preB 300.19 cells towards the indicated chemokines was measured in the presence of plasma IgGs from COVID-19 convalescents (n=24) or controls (n=8). Technical triplicates (Mean±SEM) of migrated cells in 5 high-power fields (HPF). Two-tailed Mann–Whitney U-tests. (**B**) Model of the interaction between a chemokine and its receptor. Arrows point to the area of putative interaction between the N-terminus of the receptor and the chemokine N-loop (shown by spheres). Chemokine is magenta and chemokine receptor is cyan. (**C**) Characteristics of the COVID-19 cohort. (**D**) Identification of individuals with high anti-CCL8 antibodies. Top, optical density (OD_{450}) shows plasma IgG reactivity to the CCL8 N-loop peptide, as determined by ELISA. Bottom, area under the curve (AUC) of the data in top panel. Average of two independent experiments. COVID-19 convalescents (n=71); controls (n=23). Horizontal bars indicate median values. (**E**) Detection of anti-IFNα2 IgGs. Data are shown as in (D). Average AUC from two independent experiments. (**F**) CCL8 binding human B cells. Flow cytometry plots identify human B cells binding to the CCL8 N-loop peptide (gate). The frequency of antigen-specific B cells is shown. (**G**) Monoclonal antibodies to the CCL8 N-loop. ELISA binding curves of representative antibodies. Average of two independent experiments (Mean+SEM). (**H**) Chemotaxis of human monocytes towards CCL8 is inhibited by monoclonal antibodies. Mean±SEM of migrated cells in 5 high-power fields (HPF). At least 3 independent experiments with cells from different donors. Up-pointing triangle is antibody alone, and down-pointing triangle is buffer control. Two-way RM ANOVA followed by Šídák's multiple comparisons test.
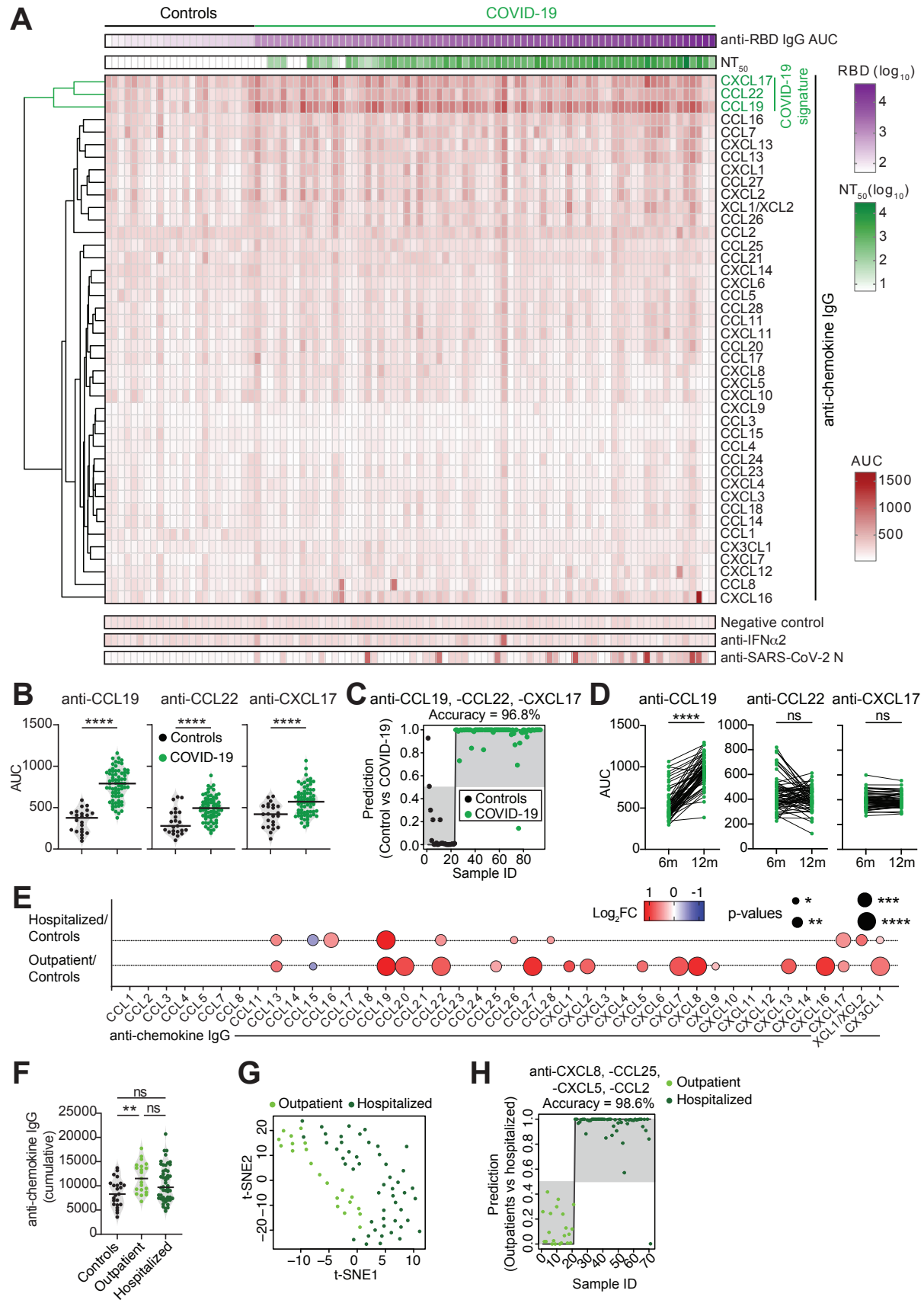
See also fig. S1; tables S1-S5.

Figure 2

Fig. 2. Distinct patterns of anti-chemokine antibodies distinguish COVID-19 convalescents with different disease severity. (**A**) Anti-chemokine antibodies 6 months after COVID-19. Heatmap representing plasma IgG binding to 42 peptides comprising the N-loop sequence of all 43 human chemokines, as determined by ELISA (AUC, average of two independent experiments). Samples are ranked according to the level of anti-SARS-CoV-2-RBD. Anti-chemokine IgG signals are ordered by unsupervised clustering analysis. SARS-CoV-2 pseudovirus neutralizing activity (NT_{50}) and IgG binding to peptides corresponding to negative control, IFNα2 and SARS-CoV-2 nucleocapsid protein (N) are shown. COVID-19 convalescents (n=71); controls (n=23). (**B**) Difference in antibodies to CCL19, CCL22 and CXCL17 (COVID-19 signature). Horizontal bars indicate median values. Two-tailed Mann–Whitney U-tests. (**C**) Assignment of COVID-19 convalescents and controls based on the COVID-19 signature antibodies by logistic regression analysis. Dots on grey background are correctly assigned. (**D**) Anti-COVID-19 signature chemokine IgG antibodies at 6 and 12 months in convalescents. AUC from two independent experiments. Wilcoxon signed-rank test. (**E**) Difference in anti-chemokine antibodies between COVID-19 groups and controls. Summary circle plot: circle size indicates significance; colors show the Log_2 fold-change increase (red) or decrease (blue) over controls. Kruskal-Wallis test followed by Dunn's multiple comparison test. (**F**) Difference in total anti-chemokine antibodies. Cumulative signal of the IgGs against the 42 peptides comprising the N-loop sequence of all 43 human chemokines. Horizontal bars indicate median values. Kruskal-Wallis test followed by Dunn's multiple comparison test. (**G**) t-SNE distribution of COVID-19 outpatient and hospitalized individuals, as determined with the 42 datasets combined. (**H**) Assignment of COVID-19 outpatient and hospitalized individuals based on the COVID-19 signature antibodies by logistic regression analysis. Dots on grey background are correctly assigned.
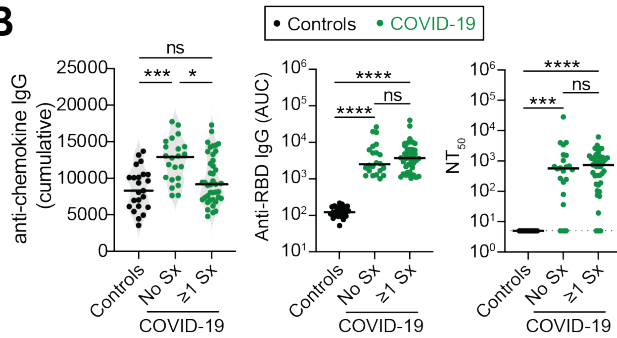
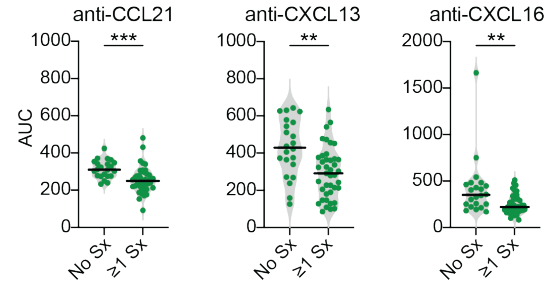See also Figs. S2-7; tables S2 and S5.

Figure 3

A

Acute disease course	n	≥1 symptom at t=12m	Average number of symptoms, if any
Outpatient (M/F)	19 (8/11)	9 (5/4)	2.9 (2.6/3.3)
Hospitalized (M/F)	44 (26/18)	32 (17/15)	3.5 (3.4/3.5)

B

anti-chemokine IgG (cumulative)

Anti-RBD IgG (AUC)

NT_{50}

- Controls
- COVID-19

C

anti-CCL21

anti-CXCL13

anti-CXCL16

AUC

D anti-CCL21, -CXCL13, -CXCL16

Accuracy = 77.8%

Prediction ("No Sx" vs "≥1 Sx" at 12m)

Sample ID

E anti-CXCL16 N-loop

$OD_{450\,nm}$

mAb concentration [ng/ml]

- isotype
- aCXCL16.001
- aCXCL16.002
- aCXCL16.003

F CXCR6

Relative migration (%)

aCXCL16.001, aCXCL16.002, aCXCL16.003, isotype

CXCL16 [1nM]

G anti-CXCL13 N-loop

$OD_{450\,nm}$

mAb concentration [ng/ml]

- isotype
- aCXCL13.001
- aCXCL13.002
- aCXCL13.003

H primary B cells
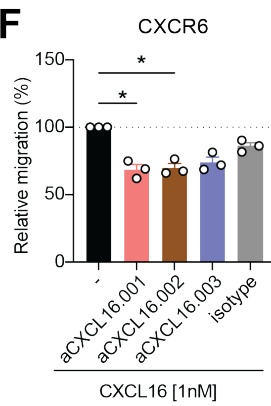
Migrated cells/5HPF

CXCL13 [nM]

- CXCL13
- CXCL13 + aCXCL13.001
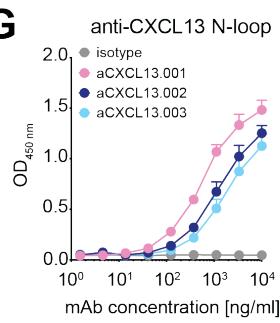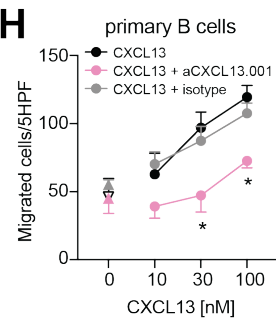- CXCL13 + isotype

Fig. 3. Long COVID and anti-chemokine antibodies. (**A**) Characteristics of the COVID-19 convalescent cohort at 12 months. (**B**) Persisting symptoms (Sx) at 12 months and anti-chemokine IgG (cumulative; left), anti-RBD IgG (middle), and NT_{50} (right) values at 6 months. Horizontal bars indicate median values. Average AUC from two independent experiments. Kruskal-Wallis test followed by Dunn's multiple comparison test. (**C**) Difference in antibodies to CCL21, CXCL13 and CXCL16 (Long COVID signature). Horizontal bars indicate median values. Average AUC from two independent experiments. Two-tailed Mann–Whitney U-tests. (**D**) Group assignment based on the Long COVID signature antibodies at 6 months against CCL21, CXCL13 and CXCL16, by logistic regression analysis. Dots on grey background are correctly assigned. (**E**) Anti-CXCL16 antibodies binding to the CXCL16 N-loop in ELISA. Average of two independent experiments (Mean+SEM). (**F**) Anti-CXCL16 N-loop antibodies inhibit CXCL16 chemotaxis to CXCR6. Relative cell migration towards CXCL16 by cells uniquely expressing CXCR6 (see Methods). Mean+SEM of 3 independent experiments. Kruskal-Wallis test followed by Dunn's multiple comparison test. (**G**) Anti-CXCL13 antibodies binding to the CXCL13 N-loop in ELISA. Average of two independent experiments (Mean+SEM). (**H**) The anti-CXCL13 N-loop antibody aCXCL13.001 inhibits CXCL13 chemotaxis of primary CD19^{+} human B cells. Mean±SEM of migrated cells in 5 high-power fields (HPF). The average of 3 independent experiments with cells from different donors is shown. Up-pointing triangles indicate antibody alone, and down-pointing triangle is buffer control. Two-way RM ANOVA followed by Šídák's multiple comparisons test.

See also fig. S8; tables S3-S5.

Figure 4
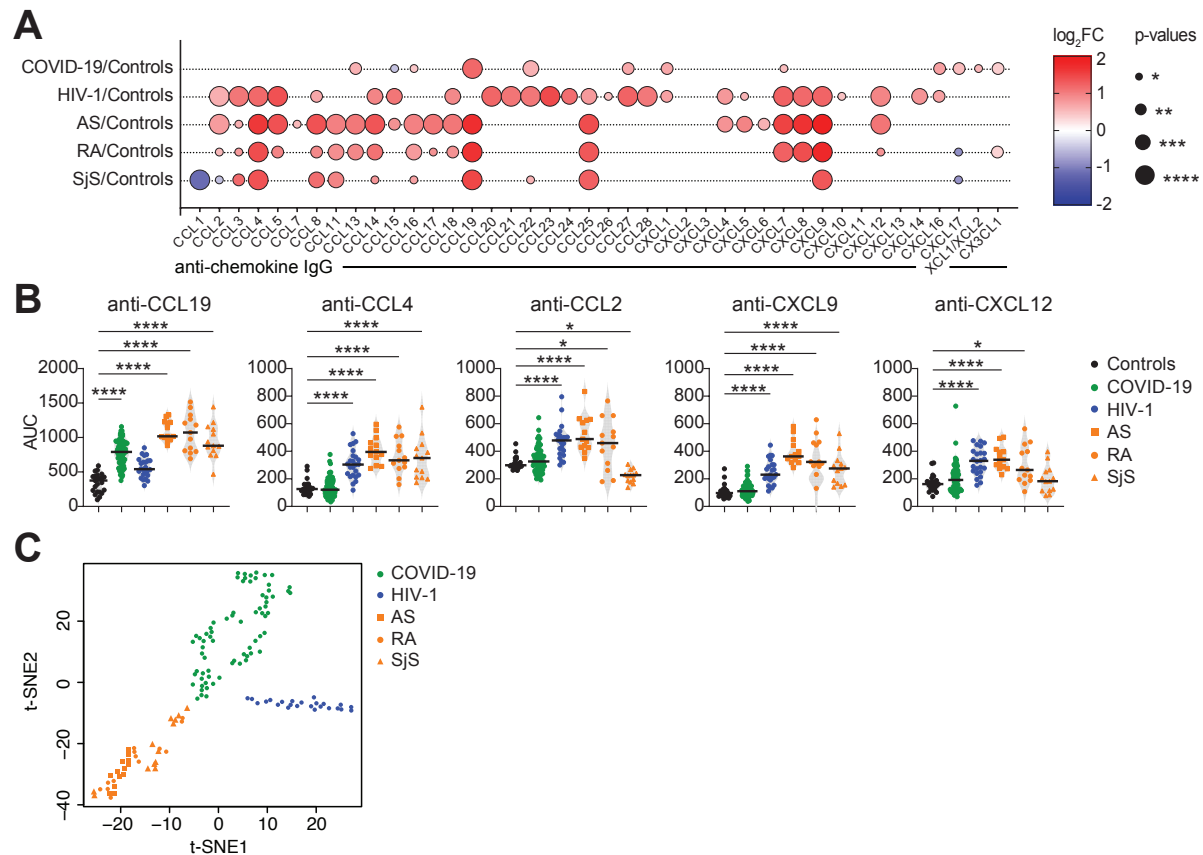
Fig. 4. Distinct patterns of anti-chemokine antibodies in COVID-19, HIV-1 or autoimmune diseases. (**A**) Difference in anti-chemokine antibodies between disease groups and controls. Summary circle plot: circle size indicates significance; colors show the Log$_2$ fold-change increase (red) or decrease (blue) over controls. Kruskal-Wallis test followed by Dunn's multiple comparison test. (**B**) Difference in antibodies to CCL19, CCL4, CCL2, CXCL9 and CXCL12 across groups. Controls (n=23), COVID-19 (n=71), HIV-1 (n=24), Ankylosing Spondylitis (AS, n=13), Rheumatoid Arthritis (RA, n=13), and Sjögren's syndrome (SjS, n=13). Horizontal bars indicate median values. Average AUC from two independent experiments. Kruskal-Wallis test followed by Dunn's multiple comparison test over rank of the control group. (**C**) t-SNE distribution of the different disease groups, as determined with the 42 datasets combined.

See also figs. S9 and 10; table S5.

MATERIAL AND METHODS

Major Resources Table

REAGENT or RESOURCE	SOURCE	IDENTIFIER
Antibodies		
Anti-human CD14, APC-eFluor780, clone 61D3	Thermo Fisher Scientific	Cat#47-0149-42; RRID:AB_1834358
Anti-human CD16, APC-eFluor780, clone eBioCB16 (CB16)	Thermo Fisher Scientific	Cat#47-0168-41; RRID:AB_11219083
Anti-human CD20, PE-Cy7, clone L27 (IVD)	BD Biosciences	Cat#335828; RRID:AB_2868689
Anti-human CD3, APC-eFluor780, clone OKT3	Thermo Fisher Scientific	Cat#47-0037-41; RRID:AB_2573935
Anti-human CD8a, APC-eFluor780, clone OKT8	Thermo Fisher Scientific	Cat#47-0086-42; RRID:AB_2573945
Anti-human IgG, HRP-linked whole Ab	GE Healthcare	Cat# NA933; RRID:AB_772208
mAb aCCL8.001	This paper	n/a
mAb aCCL8.003	This paper	n/a
mAb aCCL8.004	This paper	n/a
mAb aCCL8.005	This paper	n/a
mAb aCCL20.001	This paper	n/a
mAb aCXCL13.001	This paper	n/a
mAb aCXCL13.002	This paper	n/a
mAb aCXCL13.003	This paper	n/a
mAb aCXCL16.001	This paper	n/a
mAb aCXCL16.002	This paper	n/a
mAb aCXCL16.003	This paper	n/a
mAb Z021	Robbiani et al., 2017	n/a
Bacterial and virus strains		
One Shot™ TOP10 Chemically Competent *E. coli*	Thermo Fisher Scientific	Cat#C404006
Biological samples		
Blood Specimens of SARS-CoV-2 infected or convalescent individuals	Clinica Luganese Moncucco (CLM)	n/a
Blood Specimens of SARS-CoV-2 unexposed individuals or from pre-pandemic blood bank donors	*Institute for Research in Biomedicine (IRB)*	n/a
Plasma Specimens of COVID-19-vaccinated individuals	CLM; IRB	n/a
Plasma Specimens of HIV-1-infected individuals	Cecchinato et al., 2017	n/a
Plasma Specimens of individuals with AS or RA	University of Zurich (UZH)	n/a
Plasma Specimens of individuals with SjS	IRCCS San Matteo	n/a
Blood Specimens from buffy coats	Swiss Red Cross	n/a
Chemicals, peptides, and recombinant proteins		
Human CCL2	Clark-Lewis et al., 1997	n/a
Human CCL7	Clark-Lewis et al., 1997	n/a
Human CCL8	Peprotech or this paper	Cat#300-15 or n/a
Human CCL20	Clark-Lewis et al., 1997	n/a
Human CXCL13	Clark-Lewis et al., 1997	n/a
Human CXCL16	Peprotech	Cat#300-55
NeutrAvidin protein	Thermo Fisher Scientific	Cat#3100
Streptavidin-Alexa Fluor-647	BioLegend	Cat#405237
Streptavidin-BV711	BD Biosciences	Cat#563262
Streptavidin-PE	Thermo Fisher Scientific	Cat#12-4317-87
Albumin from chicken egg white	Sigma-Aldrich	Cat#A5503

SARS-CoV-2 RBD	This paper	n/a
Synthetic biotinylated peptides (see Table S2)	GenScript (Hong Kong)	https://www.genscript.com/
Critical commercial assays		
EZ-Link™ Sulfo-NHS-LC-Biotinylation Kit	Thermo Fisher Scientific	Cat#21435
Pan B-cell Isolation kit (human)	Milteny Biotech	Cat#130-101-638
CD14 MicroBeads (human)	Milteny Biotech	Cat#130-050-201
CD19 MicroBeads (human)	Milteny Biotech	Cat#130-050-301
Pierce™ TMB Substrate Kit	Thermo Fisher Scientific	Cat#34021
Zombie NIR™ Fixable Viability Kit	BioLegend	Cat#*423105*
Experimental models: Cell lines		
293T$_{ACE2}$	Robbiani et al., 2020	n/a
HEK293T (ATCC CRL-11268)	Robbiani et al., 2020	n/a
Expi293F	Thermo Fisher Scientific	Cat#A14527
PreB 300.19 murine cell line expressing hCCR2	Ogilvie et al., 2001	n/a
PreB 300.19 murine cell line expressing hCCR6	Loetscher et al., 1997	n/a
PreB 300.19 murine cell line expressing hCXCR6	Loetscher et al., 1997	n/a
Oligonucleotides		
Oligonucleotides for antibody cloning	Robbiani et el., 2020	n/a
Recombinant DNA		
pCRV1-NLGagPol (pHIV-1 NLGagPol)	Schmidt et al., 2020	n/a
pNanoLuc2AGFP (pCCNG/nLuc)	Schmidt et al., 2020	n/a
pSARS-CoV-2 (2d19)	Schmidt et al., 2020	n/a
Human IgG1 heavy-chain vector	Robbiani et al., 2020	n/a
Human lambda light-chain vector	Robbiani et al., 2020	n/a
Human kappa light-chain vector	Robbiani et al., 2020	n/a
Software and algorithms		
Adobe Illustrator 2021	Adobe	https://www.adobe.com/
FlowJo Software (version 10.7.1)	Three Star	https://www.flowjo.com/
Gen5 Software	Agilent	https://www.agilent.com/
Glomax software	Promega	https://www.promega.com/
IgPipeline	Robbiani et al., 2020	https://www.github.com/stratust/igpipeline
Microsoft Excel	Microsoft Excel	https://www.microsoft.com/en-gb/
Prism 9 (version 9.0.2)	GraphPad Software	https://www.graphpad.com/scientific-software/prism/
Pretty Heatmaps (*pheatmap*) R package v 1.0.12	https://cran.r-project.org/web/packages/pheatmap/index.html	n/a
PyMOL 2.5.0	Schrödinger, Inc.	https://pymol.org
Rtsne R package v 0.15	https://cran.r-project.org/web/packages/Rtsne/	n/a
SnapGene 5.3.2	SnapGene	https://www.snapgene.com
R 4.1.1	R Development Core Team	https://www.r-project.org/
RStudio 2021.09.0	RStudio	https://www.rstudio.com/
Other		
Dimethyl sulfoxide	Sigma-Aldrich	Cat#41640
Histopaque	Sigma-Aldrich	Cat#H8889
Medium Expi293 Expression	Thermo Fisher Scientific	Cat#A1435102
Medium GIBCO FreeStyle 293 Expression	Thermo Fisher Scientific	Cat#12338026

Pasteurized Plasma Protein Solution	Swiss Red Cross Laboratory	n/a
Polyethylenimine Max PEI-MAX	Polysciences	Cat#24765-1
Protein G Sepharose™ 4 Fast Flow	Cytiva	Cat#17-0618-01P
RNasin Ribonuclease Inhibitors	Promega	Cat#N2615
RPMI 1640 Medium, Hepes, no glutamine	Thermo Fisher Scientific	Cat#42401018

Study participants and ethical approvals

COVID-19 cohort: 71 participants, who were diagnosed with COVID-19 at the Clinica Luganese Moncucco (CLM, Switzerland) between 08.03.2020 and 22.11.2020, were enrolled in the study and divided into two groups, according to the severity of the acute disease. The hospitalized group included 50 participants; the outpatient group included 21 close contacts of the hospitalized group, who only received at-home care. Inclusion criteria for the hospitalized group were a SARS-CoV-2 positive nasopharyngeal swab test by real-time reverse transcription-polymerase chain reaction (RT-PCR) and age ≥18 years. Inclusion criteria for the outpatient group were being a symptomatic close contact (living in the same household) of an individual enrolled in the hospitalized group and age ≥18 years. At the 12-month visits, participants were asked to indicate the presence or absence of persisting symptoms related to COVID-19 according to a questionnaire. The study was performed in compliance with all relevant ethical regulations and the study protocols were approved by the Ethical Committee of the Canton Ticino (ECCT): CE-3428 and CE-3960.

Control cohort: 15 adult participants (≥18 years) with self-reported absence of prior SARS-CoV-2 infection or vaccination (confirmed by negative serologic test, fig. S4A) were enrolled between November 2020 and June 2021. Additional 8 pre-pandemic samples were obtained from blood bank donors (ECCT: CE-3428).

Vaccination cohort: 16 adult participants (≥18 years) with self-reported absence of prior SARS-CoV-2 infection (confirmed by negative serologic test, fig. S5F) and who received two doses of mRNA-based COVID-19 vaccine (*65, 66*), were enrolled on the day of first vaccine dose or earlier, between November 2020 and October 2021. (ECCT: CE-3428)

HIV-1 and autoimmune diseases cohorts: Pre-pandemic plasma samples were obtained from the following participants: 24 HIV-1 positive (ECCT: CE-813) (*67*), 13 each with Ankylosing Spondylitis, Rheumatoid Arthritis (ECCT: CE-3065, and Ethical Committee of the Canton Zurich: EK-515), or Sjögren's syndrome (IRCCS Policlinico San Matteo Foundation Ethics Committee n.20070001302).

Written informed consent was obtained from all participants, and all samples were coded to remove identifiers at the time of blood withdrawal. Demographic, clinical, and serological features are reported in tables S1 and S5.

Blood collection, processing, and storage

Blood was collected by venipuncture at approximately 6 month intervals and the peripheral blood mononuclear cells (PBMCs) were isolated using Histopaque density centrifugation. Total PBMCs were aliquoted and frozen in liquid nitrogen in the presence of fetal calf serum and DMSO. Plasma was aliquoted and stored at -20ºC or less. Before use, plasma aliquots were heat-inactivated (56ºC for 1 h) and then stored at 4ºC. For chemotaxis assays, CD14$^+$ monocytes and CD19$^+$ B cells were enriched from fresh PBMCs derived from blood donors (Swiss Red Cross Laboratory; ECCT: CE-3428) through positive immunoselection (130-050-201 and 130-050-301, respectively [Miltenyi Biotec, Bergisch Gladbach, Germany]) according to the manufacturer's instructions. After isolation, CD19$^+$ B cells were rested overnight in RPMI-1640 medium supplemented with 10% (v/v) fetal bovine serum (FBS), 1% (v/v) non-essential amino acids, 1 mM sodium pyruvate, 2 mM GlutaMAX, 50 µM β-Mercaptoethanol and 50 U/ml penicillin/streptomycin (all from Gibco) before being used in chemotactic assays.

Reagents

Peptides: Synthetic peptides containing the N-loop or the C-terminal sequence of human chemokines were designed and obtained (> 75% purity) from GenScript (Hong Kong). All peptides are biotinylated (biotin-Ahx) at the N-terminus and amidated at the C-terminus. In addition, the first 2-4 amino acids of each peptide (GS, GGS, GGGS, or GGK depending on the length of the N-loop/C-terminus of the chemokine) consist of a linker between the biotin and the chemokine sequence. Peptides are generally 25 amino acids long, or between 22-25 amino acids when synthesis was problematic. The sequence of the IFNα2 peptide (7-28) was based on a previously described immunoreactive epitope in myasthenia gravis patients (*68*), and the one from the SARS-CoV-2 nucleocapsid protein (N) peptide (157-178) was described in (*69*). An irrelevant peptide was used as negative control. The amino acid sequences of all peptides in this study are listed in table S2.

Proteins: CCL2, CCL7, CCL20 and CXCL13 were synthesized using tBoc solid-phase chemistry (*70*). CCL8 and CXCL16 were obtained from Peprotech (Cat#300-15 and Cat#300-

55, respectively) or produced and purified in house. Briefly, recombinant chemokines were expressed in *E. coli*, purified from inclusion bodies by immobilized-metal affinity chromatography, and folded under N_2 protection in an arginine-containing buffer (80 mM Tris-Cl [pH 8.5], 100 mM NaCl, 0.8 M arginine, 2 mM EDTA, 1 mM cysteine, 0.2 mM cystine) as

5 previously described (*71*). After recovery and concentration, the purification tag was cleaved with enterokinase, and the processed chemokine was purified by C_{18} reverse phase chromatography. The SARS-CoV-2 receptor binding domain (RBD) was produced and purified as described (*72*).

10 ***Chemotaxis***

The migration of primary human monocytes and B cells isolated from buffy coats, or of murine preB 300.19 cells stably expressing the human chemokine receptors CCR2 (*73*), CCR6 and CXCR6 (*74*) was assayed using 48-well Boyden chambers (Neuro Probe, Cabin John, MD) with polyvinylpyrrolidone-free polycarbonate membranes with pore size of 3 μm for primary

15 human B cells and 5 μm for the other cell types, as previously described (*44*). Briefly, 10^5 primary human B cells or 5×10^4 primary human monocytes and murine preB 300.19 cells were diluted in RPMI-1640 supplemented with 20 mM Hepes, pH7.4, and 1% pasteurized plasma protein solution (5% PPL SRK; Swiss Red Cross Laboratory, Bern, Switzerland). Cells were then added to the upper wells and the chemokine (with or without antibodies) to the bottom

20 wells. After 120 min of incubation for primary human B cells and 90 min for the other cell types, the membrane was removed, washed on the upper side with phosphate-buffered saline (PBS), fixed, and stained with DiffQuik. All assays were done in triplicate, and for each well the migrated cells were counted at 100-fold magnification in 5 randomly selected high-power fields (5HPF).

25 Inhibition of chemotaxis by plasma purified IgGs (Fig. 1A): IgGs were purified from a subset of samples of the COVID-19 and uninfected control cohorts using Protein G Sepharose 4 Fast Flow (Cytiva) according to manufacturer's instructions (plasma:resuspended beads at a 5:4 [v/v] ratio), buffer-exchanged and concentrated in PBS by Amicon Ultra-4 centrifugal filters (30 kDa cutoff, Millipore). Chemotaxis was performed with preB 300.19 expressing CCR2, at

30 a final IgG concentration of 200 μg/ml, in the presence of the chemokine concentration resulting in peak migration when no antibodies were added (CCL2 [10nM], CCL7 [100nM], CCL8 [100nM]).

Inhibition of chemotaxis by monoclonal antibodies (Fig. 1H, and Fig. 3, F and H; fig. S1E): Experiments were performed with monoclonal antibodies at a final concentration of 30 µg/ml (Fig. 1H) or 50 µg/ml (Fig. 3, F and H; fig. S1E). Baseline migration was determined in the absence of chemoattractant (buffer control).

ELISA

To evaluate the antibodies' binding to chemokine peptides, 96-well plates (ThermoFisher, 442404) were coated with 50 µl per well of a 2µg/ml Neutravidin (Life Technologies, 31000) solution in PBS, overnight at room temperature. Plates were washed 4 times with washing buffer (PBS + 0.05% Tween-20 [Sigma-Aldrich]) and incubated with 50 µl per well of a 50 nM biotinylated peptide solution in PBS for 1 h at room temperature. After washing 4 times with washing buffer, plates were incubated with 200 µl per well of blocking buffer (PBS + 2% BSA + 0.05% Tween-20) for 2 h at room temperature. Plates were then washed 4 times with washing buffer, and serial dilutions of monoclonal antibodies or plasma were added in PBS + 0.05% Tween-20 and incubated for 1 h at room temperature. To screen for the presence of anti-chemokine IgGs, plasma samples were assayed (unless otherwise stated) at 1:50 starting dilution followed by 3 fourfold serial dilutions (1:200, 1:800, 1:3200). Monoclonal antibodies were tested at 5 µg/ml starting concentration followed by 11 threefold serial dilutions. Plates were subsequently washed 4 times with washing buffer and incubated with anti-human IgG secondary antibody conjugated to horseradish peroxidase (HRP) (GE Healthcare, NA933) at a 1:5000 dilution in PBS + 0.05% Tween-20. Finally, after washing 4 times with washing buffer, plates were developed by the addition of 50 µl per well of the HRP substrate TMB (ThermoFisher, 34021) for 9 min. The developing reaction was stopped with 50 µl per well of a 1 M H_2SO_4 solution, and absorbance was measured at 450 nm with an ELISA microplate reader (BioTek) with Gen5 software. A positive control (broadly reactive plasma from donor CLM70) and a negative control (uninfected participant) samples were included in each experiment. The Area Under the Curve (AUC) was obtained from two independent experiments and plotted with GraphPad Prism. The main findings were further confirmed by assaying subsets of samples belonging to the different groups, side-by-side on the same plates (data not shown).

Reactivity at 6 versus 12 months (fig. S5, B and C): Experiments were performed with the samples side-by-side on the same plate. In fig. S5B, plasma samples were assayed at a 1:50 starting dilution, followed by 4 additional fivefold dilutions. Anti-RBD IgG levels are shown

in COVID-19 convalescents, who have not received a COVID-19-mRNA vaccine between first and second visit (no vaccination) or in individuals with at least one dose of vaccine at least 10 days before blood sampling at the second visit (fig. S5B; see table S1).

Kinetic of signature anti-chemokine IgG antibodies (fig. S5E): Experiments were performed with plasma samples assayed at a 1:50 dilution side-by-side on the same plate, and the average optical density at 450 nm obtained from two independent experiments was plotted with GraphPad Prism.

Antibodies' binding to SARS-CoV-2 RBD (Figs. 2A, 3B; Figs. S4A, S4C, S4D, S5B, S5F and S7A): Experiments were performed with 96-well plates coated with 50 μl per well of a 5 μg/ml protein solution in PBS overnight at room temperature, and subsequently blocked and treated as described above. In this case, plasma samples were assayed either at a 1:50 starting dilution followed by 7 additional threefold serial dilutions (Figs. 2A and 3B; Figs. S4A, S4C, S4D and S7A) or followed by 3 additional fivefold serial dilutions (Fig. S5, B and F).

Single cell sorting by flow cytometry

B cells were enriched from PBMCs of uninfected controls or of COVID-19 convalescent individuals 6 months after COVID-19 (participant CLM9 for anti-CCL8 antibodies; CLM64 for anti-CCL20 antibodies; CLM5, CLM7 and CLM33 for anti-CXCL13 antibodies; and CLM8 and CLM30 for anti-CXCL16 antibodies), using the pan-B-cell isolation kit according to manufacturer's instructions (Miltenyi Biotec, 130-101-638). The enriched B cells were subsequently stained in FACS buffer (PBS + 2% FCS + 1mM EDTA) with the following antibodies/reagents (all 1:200 diluted) for 30 min on ice: anti-CD20-PE-Cy7 (BD Biosciences, 335828), anti-CD14-APC-eFluor 780 (Thermo Fischer Scientific, 47-0149-42), anti-CD16-APC-eFluor 780 (Thermo Fischer Scientific, 47-0168-41), anti-CD3-APC-eFluor 780 (Thermo Fischer Scientific, 47-0037-41), anti-CD8-APC-eFluor 780 (Invitrogen, 47-0086-42), Zombie NIR (BioLegend, 423105), as well as fluorophore-labeled ovalbumin (Ova) and N-loop peptides. Live single Zombie-NIR$^-$CD14$^-$CD16$^-$CD3$^-$CD8$^-$CD20$^+$Ova$^-$N-loop-PE$^+$N-loop-AF647$^+$ B cells were single-cell sorted into 96-well plates containing 4 μl of lysis buffer (0.5× PBS, 10 mM DTT, 3,000 units/ml RNasin Ribonuclease Inhibitors [Promega, N2615]) per well using a FACS Aria III, and the analysis was performed with FlowJo software. The anti-CCL20 antibody sequences were obtained by sorting with a pool of 12-peptides; for all the others, a single peptide was used. The sorted cells were frozen on dry ice and stored at −80 °C.

Antibody sequencing, cloning, production and purification

Antibody genes were sequenced, cloned and expressed as previously reported (*75-77*). Briefly, reverse-transcription of RNA from FACS-sorted single cells was performed to obtain cDNA, which was then used for amplification of the immunoglobulin IGH, IGK and IGL genes by nested PCR. Amplicons from this first PCR reaction served as templates for sequence and ligation independent cloning (SLIC) into human IgG1 antibody expression vectors. Monoclonal antibodies were produced by transiently transfecting Expi293F cells cultured in Freestyle-293 Expression Medium (ThermoFisher) with equal amounts of Ig heavy and light chain expression vectors using polyethylenimine Max (PEI-MAX, Polysciences) as a transfection reagent. After 6-7 days of culture, cell supernatants were filtered through 0.22 μm Millex-GP filters (Merck Millipore), and antibodies were purified using Protein G Sepharose 4 Fast Flow (Cytiva) according to manufacturer's instructions and buffer-exchanged and concentrated in PBS by Amicon Ultra-4 centrifugal filters (30 kDa cutoff, Millipore). Where indicated, the anti-Zika virus monoclonal antibody Z021 (*75*) was used as an isotype control.

Computational analysis of antibody sequences

Antibody sequences were analyzed using a collection of Perl and R scripts provided by IgPipeline and publicly available on GitHub (https://github.com/stratust/igpipeline) (*47*). In brief, sequences where annotated using IgBlast (*78*) v 1.14.0 with IMGT domain delineation system and the Change-O toolkit v 0.4.5 (*79*). Nucleotide somatic hypermutation and CDR3 were determined by aligning the IGHV and IGLV nucleotide sequence against their closest germlines using the blastn function of IgBlast. Differences outside CDR3 were considered as mutations.

SARS-CoV-2 pseudotyped reporter virus and neutralization assay

To generate (HIV-1/NanoLuc2AEGFP)-SARS-CoV-2 particles, HEK293T cells were co-transfected with the three plasmids pHIV$_{NL}$GagPol, pCCNanoLuc2AEGFP, and SARS- CoV-2 S as described elsewhere (*47, 80*). Supernatants containing virions were collected 48 h after transfection, and virion infectivity was determined by titration on 293T$_{ACE2}$ cells. The plasma neutralizing activity was measured as previously reported (*47, 80*). Briefly, threefold serially diluted plasma samples (from 1:50 to 1:328'050) were incubated with SARS-CoV-2 pseudotyped virus for 1h at 37 °C, and the virus-plasma mixture was subsequently incubated

with $293T_{ACE2}$ cells for 48 h. Cells were then washed with PBS and lysed with Luciferase Cell Culture Lysis 5× reagent (Promega). Nanoluc Luciferase activity in cell lysates was measured using the Nano-Glo Luciferase Assay System (Promega) with Modulus II Microplate Reader User interface (TURNER BioSystems). The obtained relative luminescence units were normalized to those derived from cells infected with SARS-CoV-2 pseudotyped virus in the absence of plasma. The NT_{50} values were determined using four-parameter nonlinear regression with bottom and top constrains equal to 0 and 1, respectively (GraphPad Prism). The dotted line (NT_{50}=5) in the plots represents the lower limit of detection of the assay.

Model interaction between chemokine and chemokine receptor

The illustrative model in Fig. 1 was generated from the structure of inactive CCR2 (PDB code: 5T1A) (*81*), together with the electron microscopy structures of CCR5 and CCR6 (PDB codes: 6MEO and 6WWZ, respectively (*82, 83*) by using SWISS-MODEL (*84*) server and the molecular graphics program PyMOL 2.5.0 for modeling the N- and C-terminus of the receptor. The crystal structure of CCL8 (MCP-2) (PDB code: 1ESR) (*85*), and the electron microscopy structure of CCR6 (*83*) were used to model the complex. The intracellular residues were removed for clarity.

Statistical analysis

Tests for statistical significance: Statistical significance between two groups was determined using non-parametric two-tailed Mann–Whitney U-tests, or Wilcoxon signed-rank test, for unpaired or paired samples, respectively. Upon testing of parametric assumptions, statistical significance between more than two groups was evaluated using Kruskal-Wallis test (followed by Dunn multiple comparisons), one-way ANOVA (followed by Tukey multiple comparisons), or two-way Repeated Measures ANOVA (followed by Šídák multiple comparisons), as described in the figure legends. Statistical significance of the signature chemokines (CCL19, CCL22, CXCL17, CXCL8, CCL25, CXCL5, CCL21, CXCL13 and CXCL16) was also confirmed when applying the Bonferroni criterion in order to guarantee a familywise level of significance equal to 0.05. Statistical significance from a 2x2 contingency table was determined with Fisher's exact test. Correlations were assessed using Pearson correlation analysis. A p-value of less than 0.05 was considered statistically significant. In the figures, significance is shown as follow: ns $p \geq 0.05$ (not significant), *$p<0.05$, **$p<0.01$, ***$p<0.001$ and ****$p<0.0001$. Data and statistical analyses were performed with GraphPad Prism.

t-SNE: t-SNE analysis was performed using the Rtsne R package v 0.15 (https://CRAN.R-project.org/package=Rtsne) using the AUC values for all chemokines. The theta parameter for the accuracy of the mapping was set to zero in all cases for exact TSNE.

Clustering: Hierarchical clustering was created using the hclust R function v 4.1.1. Clustering

5   analysis was performed using the correlation as distance and the Ward's method as agglomerative criterion. Heatmaps were created with either GraphPad Prism (Fig. 2A; fig. S3D) or the *Pretty Heatmaps* (*pheatmap*) R package v 1.0.12 (fig. S10B). In fig. S10B, each column containing a distinct chemokine was scaled with the scaling function provided by R, which sets the mean and the standard deviation to 0 and 1, respectively.

10 Logistic regression: It was performed using the GLM (Generalized Linear Models) function provided by the R package v 4.1.1. To identify which variables to include in the analysis, AUCs were ranked according to the p-value obtained with a Mann-Whitney parametric test. The first N variables minimizing the AIC (Akaike information criterion) were then used in the fitting. In each plot, values from 0 to 0.5 and from 0.5 to 1 on the y-axis represent the assignment of

15 individuals to the A and B groups (of a Prediction A versus B; see grey backgrounds), respectively. On the x-axis, samples are divided into the two groups and subsequently ordered according to sample ID as shown in table S1. Dots in the grey area represent individuals that are assigned to the correct group.
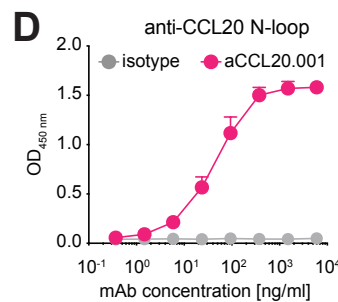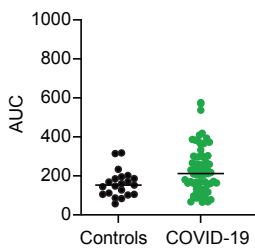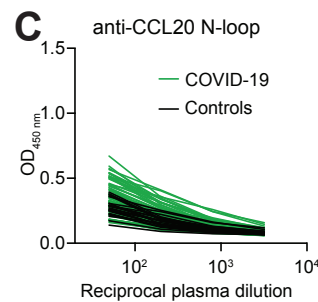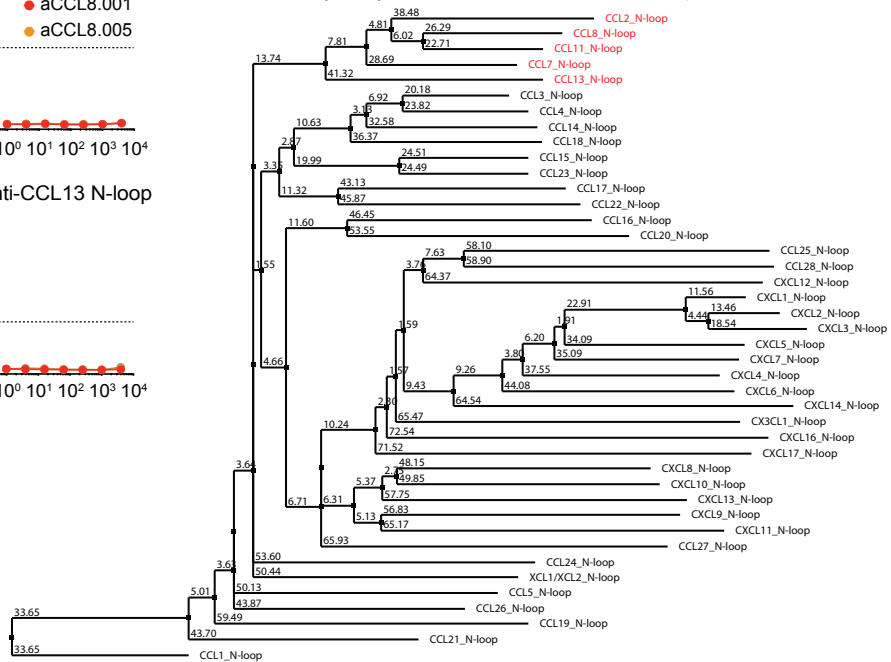
20

Figure S1
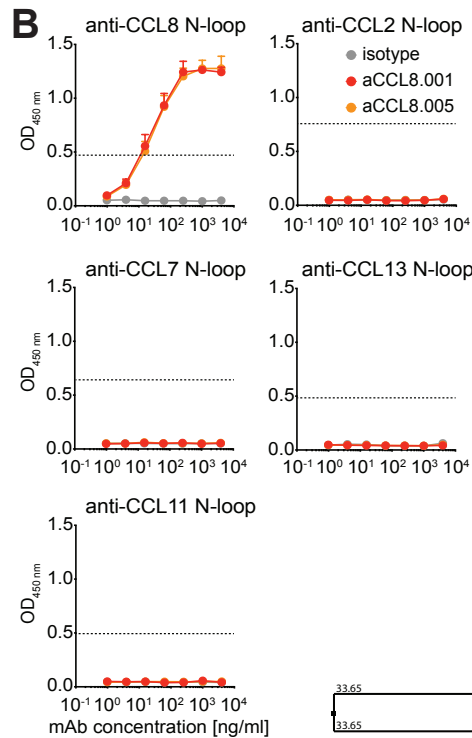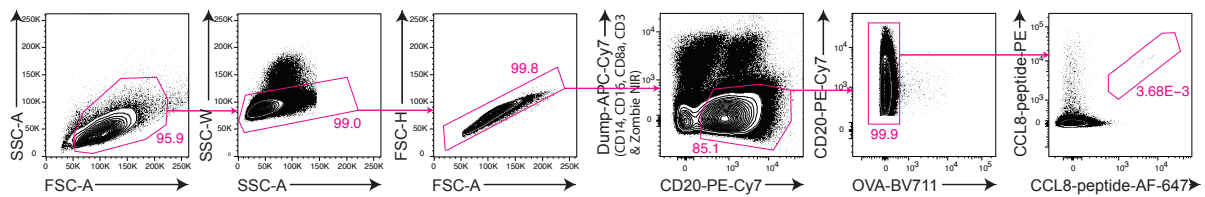
Fig. S1. Identification and specificity of anti-CCL8 antibodies, related to Fig. 1. (**A**) Gating strategy for sorting CCL8 N-loop specific B cells by flow cytometry. (**B**) Anti-CCL8 antibodies bind the CCL8 N-loop specifically. Similarity analysis of all human chemokines N-loops by Neighbour joining-BLOSUM62 identifies those that are most similar to CCL8 (red in the right panel). Anti-CCL8 antibodies with VH4-39/VK4-1 only bind to CCL8 in ELISA (left panel). Dashed lines indicate the signal of a positive control plasma sample with broad reactivity (CLM70). Average of two independent experiments (Mean+SEM). (**C**) Identification of individuals with high anti-CCL20 antibodies. Right, optical density (OD_{450}) shows plasma IgG reactivity to the CCL20 N-loop peptide, as determined by ELISA. Left, area under the curve (AUC) of the data in top panel. Average of two independent experiments. COVID-19 convalescents (n=71); controls (n=23). Horizontal bars indicate median values. (**D**) ELISA Monoclonal antibodies to the CCL20 N-loop. ELISA binding curves of representative antibodies. Average of two independent experiments (Mean+SEM). (**E**) Anti-CCL20 N-loop antibodies inhibit CCL20 chemotaxis to CCR6. Relative cell migration towards CCL20. Mean+SEM of at least 3 independent experiments. Two-tailed Mann–Whitney U-tests.
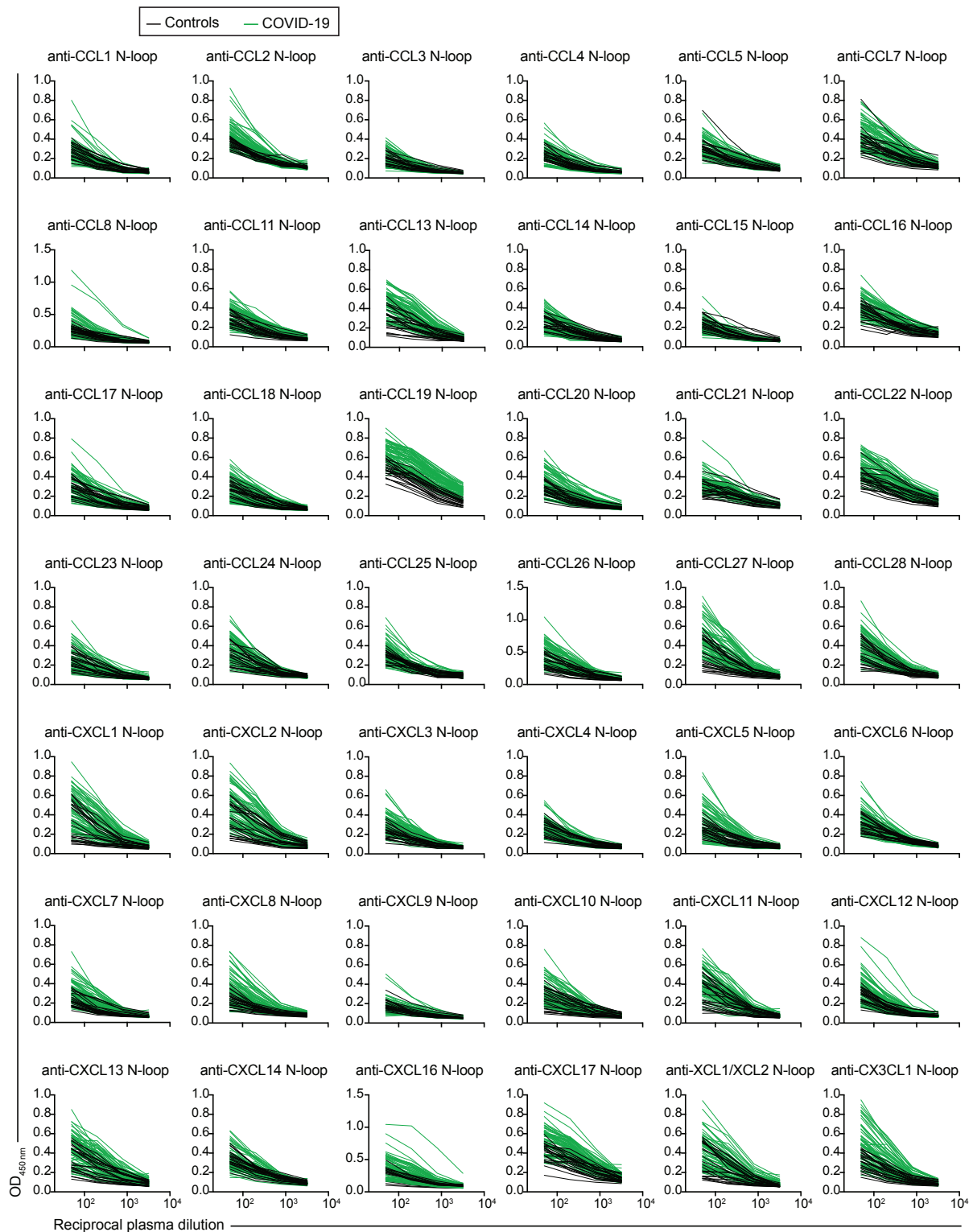
Figure S2

Fig. S2. Anti-chemokine N-loop antibodies in COVID-19, related to Fig. 2. The amount of plasma IgG antibodies against each chemokine N-loop was determined by ELISA for COVID-19 convalescents (n=71) and controls (n=23). Average optical density (OD_{450}) measurements of two independent experiments.
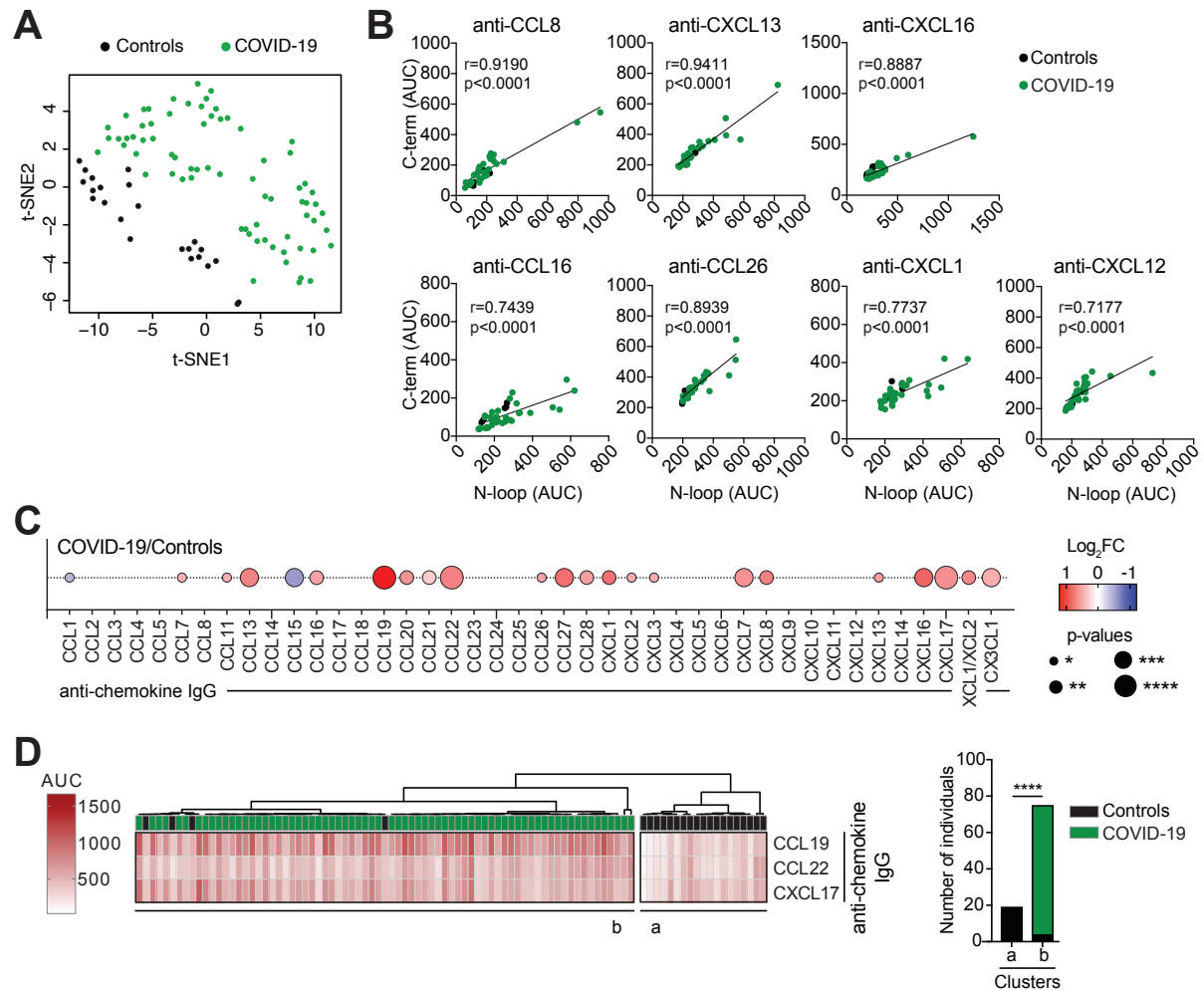
5

Figure S3

Fig. S3. Clustering analyses of anti-chemokine antibodies, related to Fig. 2. (A) t-SNE distribution of COVID-19 convalescents and controls, as determined with the 42 datasets combined. (**B**) Pearson correlations of antibodies to the N-loop and C-term peptides of the same chemokine. ELISA was performed in a cohort subset (Controls, n=5; COVID-19, n=31). Average of two independent experiments. (**C**) Differences in anti-chemokine antibodies between groups. Summary circle plot: circle size indicates significance; colors show the Log$_2$ fold-change increase (red) or decrease (blue) in the COVID-19 group over control. Two-tailed Mann–Whitney U-tests. (**D**) Antibodies to CCL19, CCL22 and CXCL17 correctly classify COVID-19 convalescents versus controls. Unsupervised hierarchical clustering analysis with the COVID-19 signature antibodies. The distribution of the groups within each cluster is also shown. Fisher's exact test.
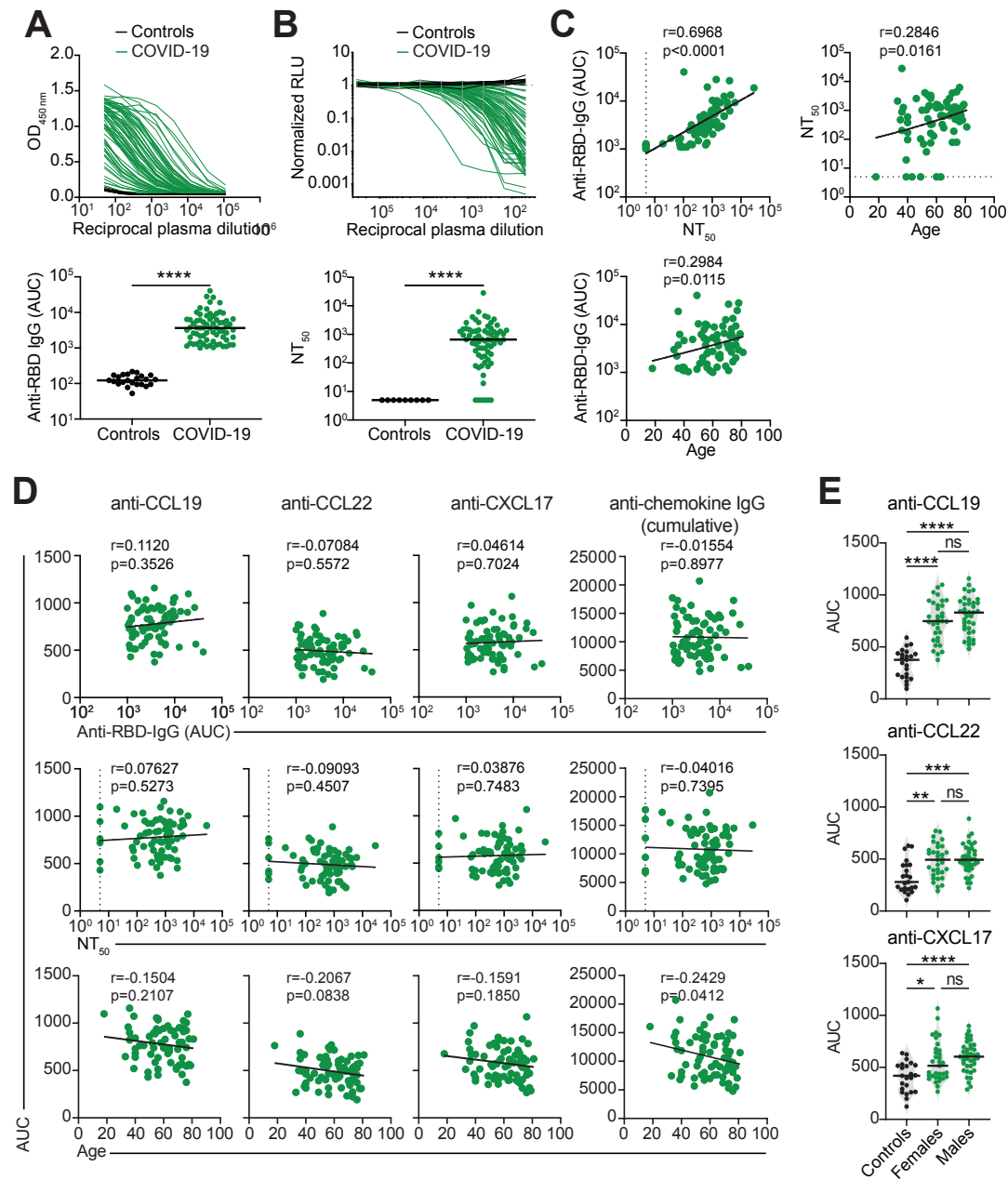
Figure S4

Fig. S4. Correlation analyses of COVID-19 signature anti-chemokine antibodies, related to Fig. 2. (**A**) Anti-RBD IgG antibodies in the cohort samples. Top, optical density reactivity (OD_{450}) of serial plasma dilutions to the receptor binding domain (RBD) of SARS-CoV-2 Spike, as determined by ELISA. Bottom, AUC of the data in the top panel. COVID-19 convalescents (n=71); controls (n=23). Average of two independent experiments. Horizontal bars indicate median values. Two-tailed Mann–Whitney U-tests. (**B**) Plasma neutralizing activity against SARS-CoV-2 pseudovirus. Top, relative luciferase units (RLU) normalized to no plasma control. Bottom, half-maximal neutralizing titers (NT_{50}) based on the data in the top panel. COVID-19 convalescents (n=71); controls (n=9). Average of two independent experiments. Horizontal bars indicate median values. Two-tailed Mann–Whitney U-tests. (**C**) Pearson correlations of anti-RBD IgG and NT_{50} values to each other and with age. Average of two independent experiments. (**D**) Pearson correlations of anti-chemokine IgG with anti-RBD IgG, NT_{50} values and age. COVID-19 signature antibodies individually, and cumulative signal of the IgGs against the peptides for all 43 chemokines. (**E**) Analysis of anti-signature chemokines IgG by gender. Data are shown as average AUC of two independent experiments. Horizontal bars indicate median values. Kruskal-Wallis test followed by Dunn's multiple comparison test.
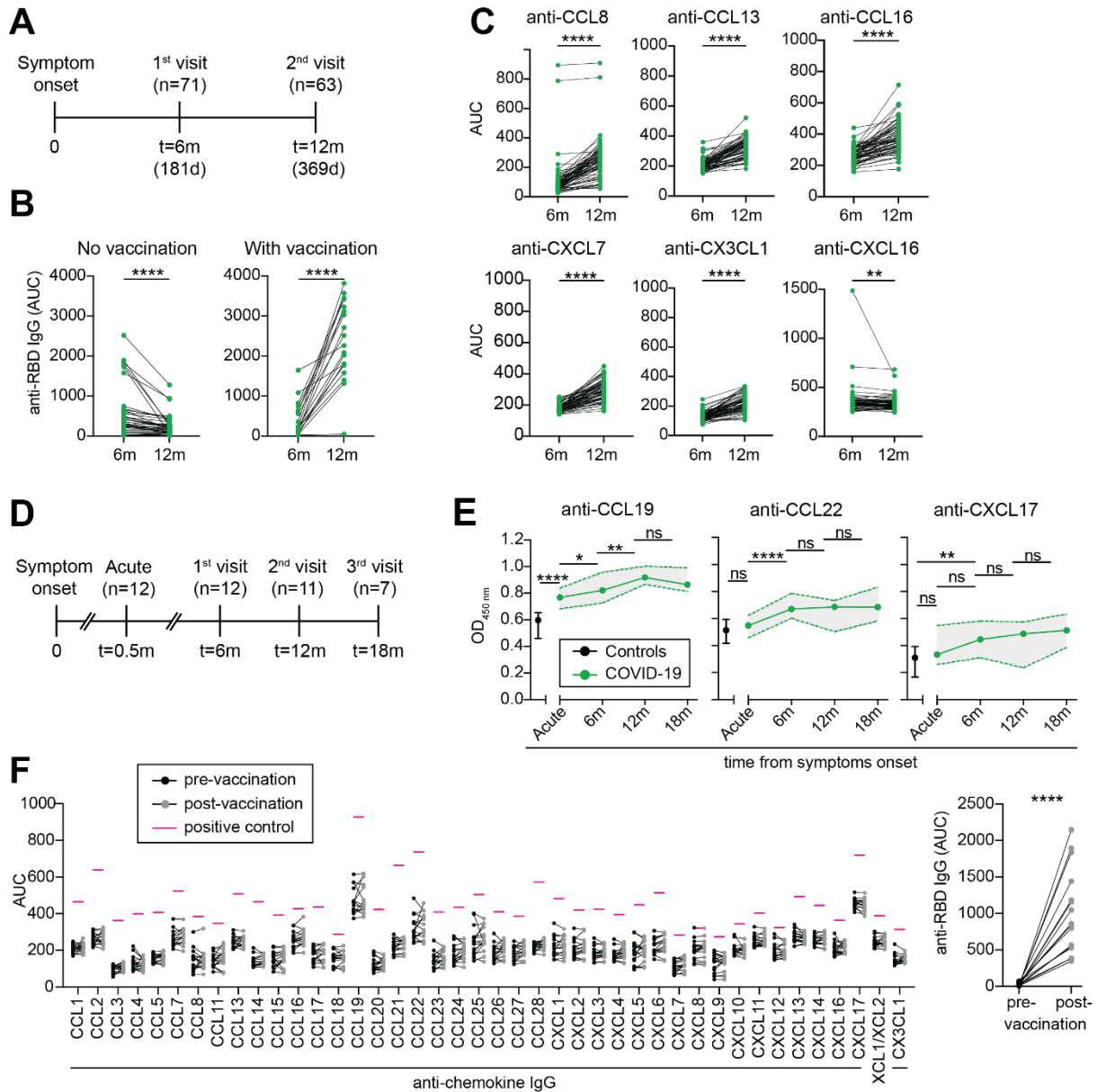
Figure S5

Fig. S5. Anti-chemokine antibodies over time and upon COVID-19 vaccination, related to Fig. 2. (**A**) Diagram of the time points of blood collection after onset of COVID-19 symptoms. (**B**) Anti-RBD IgG antibodies at 6 and 12 months in vaccinated and non-vaccinated convalescents, as determined by ELISA. Average AUC from two independent experiments. Wilcoxon signed-rank test. (**C**) Anti-chemokine IgG antibodies at 6 and 12 months in convalescents. AUC from two independent experiments. Wilcoxon signed-rank test. (**D**) Diagram of the time points of blood collection after onset of COVID-19 symptoms in a subset of COVID-19 hospitalized individuals. (**E**) Anti-chemokine IgG antibodies at 15 days (Acute), 6, 12 and 18 months after onset of COVID-19 symptoms. Average optical density (OD$_{450}$) values from two independent experiments. One-way ANOVA test followed by Tukey's multiple comparison test. Data are shown as median±range. (**F**) Anti-chemokine IgG antibodies before and approximately 4 months after COVID-19 mRNA vaccination of uninfected individuals (n=16). AUC from two independent experiments. Pink lines represent the signal of a positive control plasma sample with broad reactivity (CLM70). Anti-RBD IgG is shown alongside as control (right panel). Wilcoxon signed-rank test with false discovery rate (FDR) approach.
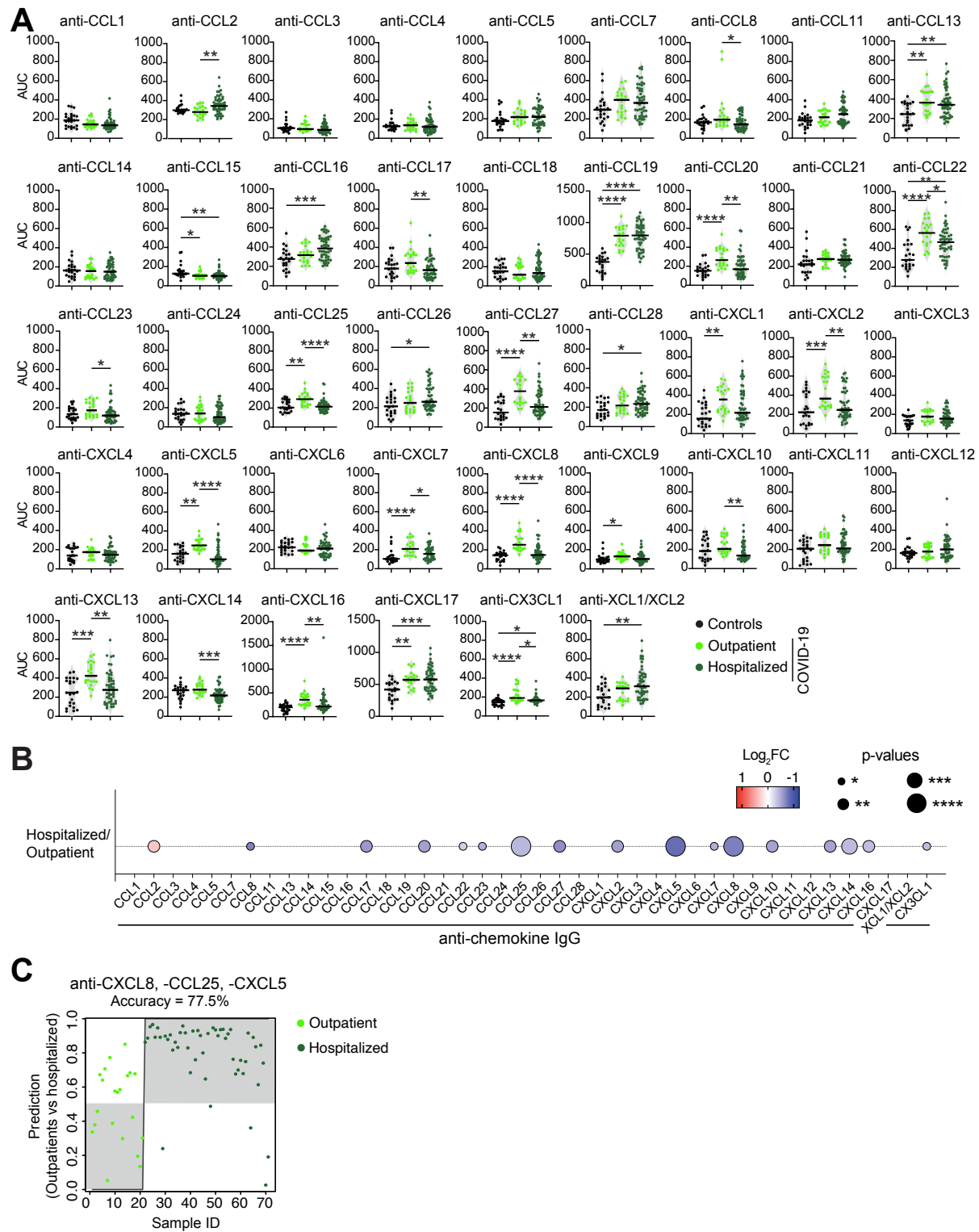
Figure S6

Fig. S6. Anti-chemokine antibodies in COVID-19 outpatient and hospitalized individuals at six months after the infection, related to Fig. 2. (**A**) Difference in anti-chemokine antibodies in outpatient versus hospitalized individuals at 6 months. Average AUC of two independent experiments. Horizontal bars indicate median values. Kruskal-Wallis test followed by Dunn's multiple comparison test. (**B**) Difference in anti-chemokine antibodies between COVID-19 outpatient and hospitalized individuals. Summary circle plot: circle size indicates significance; colors show the Log_2 fold-change increase (red) or decrease (blue) over outpatients. Kruskal-Wallis test followed by Dunn's multiple comparison test. (**C**) Group assignment based on the antibodies against CXCL8, CCL25 and CXCL5, by logistic regression analysis. Dots on grey background are correctly assigned.

Figure S7
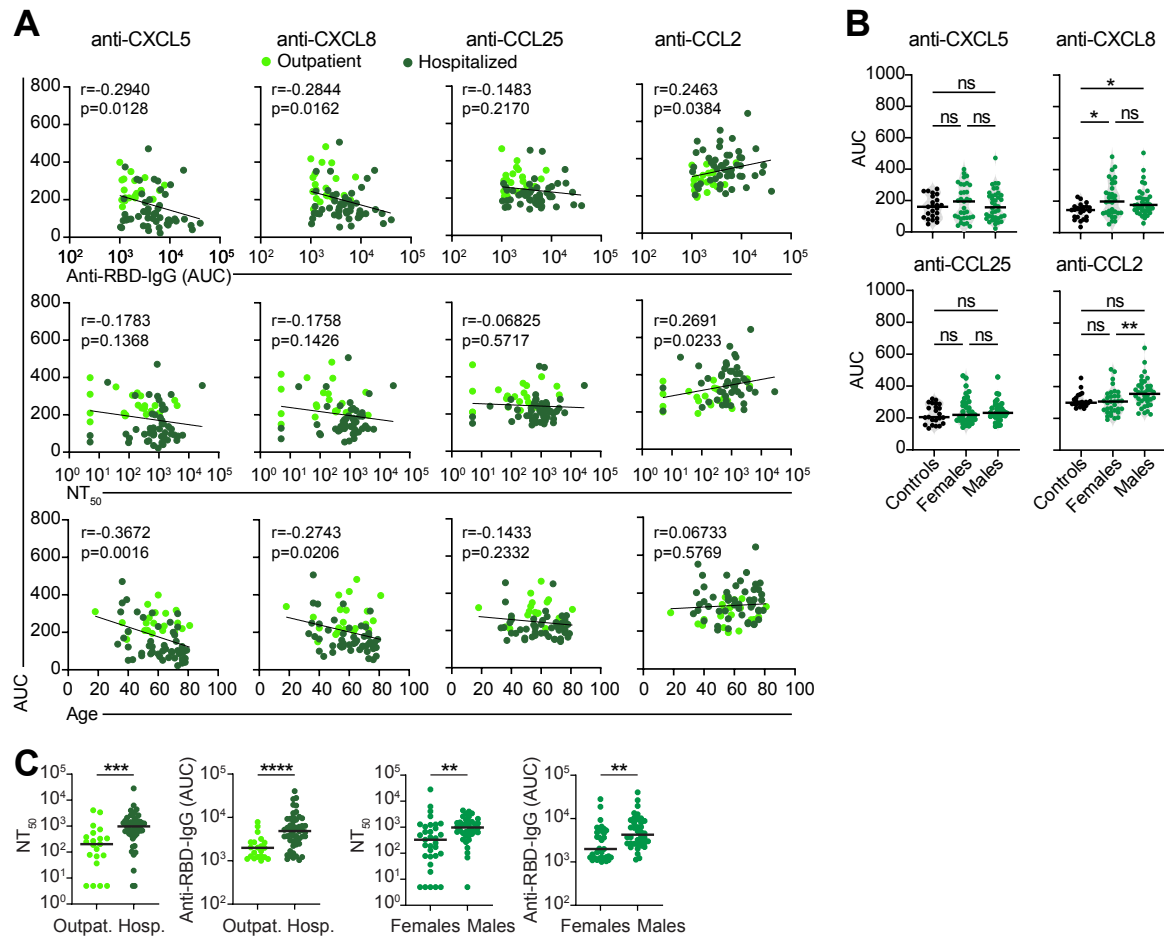
Fig. S7. Correlation analyses of COVID-19 hospitalization signature antibodies, related to Fig. 2. (**A**) Pearson correlations of anti-chemokine IgGs with anti-RBD IgG, NT_{50} values and age. COVID-19 hospitalization signature antibodies individually. Average of two independent experiments. (**B**) Analysis of anti-signature chemokine IgGs by gender. Data are shown as average AUC of two independent experiments. Horizontal bars indicate median values. Kruskal-Wallis test followed by Dunn's multiple comparison test. (**C**) Analysis of anti-RBD IgG and NT_{50} values by group and by gender. Average of two independent experiments. Horizontal bars indicate median values. Two-tailed Mann–Whitney U-tests.
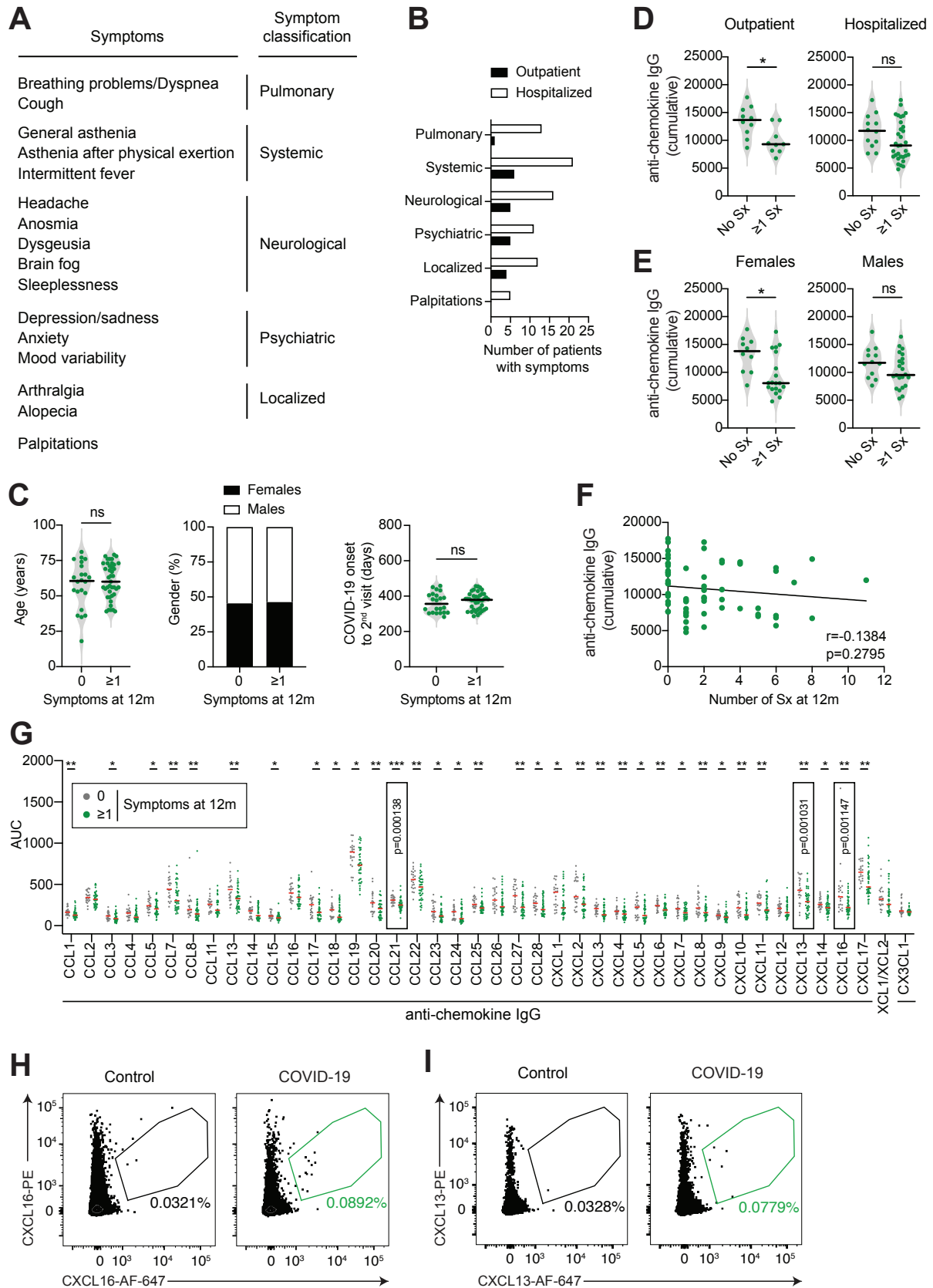
Figure S8

Fig. S8. Anti-chemokine antibodies and long-term COVID-19 symptoms, related to Fig. 3. (**A**) Classification of long-term COVID-19 symptoms at 12 months (t=12m). (**B**) Incidence of symptoms at 12 months. Participants are grouped in outpatient and hospitalized individuals. (**C**) Analysis of age (left), gender distribution (middle) and time from COVID-19 onset to 2nd visit (t=12m; right panel). Horizontal bars indicate median values. Two-tailed Mann–Whitney U-tests. (**D,E**) Difference in cumulative anti-chemokine antibodies according to the presence or absence of symptoms at 12 months in disease severity groups (D) or by gender (E). Data are shown as average AUC of two independent experiments. Horizontal bars indicate median values. Two-tailed Mann–Whitney U-tests. (**F**) Pearson correlation of anti-chemokine antibodies and the number of symptoms at 12 months. Average of two independent experiments. (**G**) Difference in anti-chemokines antibodies at 6 months and the presence or absence of symptoms at 12 months. Data are shown as average AUC of two independent experiments. Horizontal bars indicate median values. Two-tailed Mann–Whitney U-tests. The exact P-value is given for the 3 chemokines displaying the highest significance. (**H**) Human B cells specific for CXCL16. Representative flow cytometry plots identifying human B cells binding to the CXCL16 N-loop peptide (gate). The frequency of antigen-specific B cells is shown. (**I**) Human B cells specific for CXCL13. Representative flow cytometry plots identifying human B cells binding to the CXCL13 N-loop peptide (gate). The frequency of antigen-specific B cells is shown.
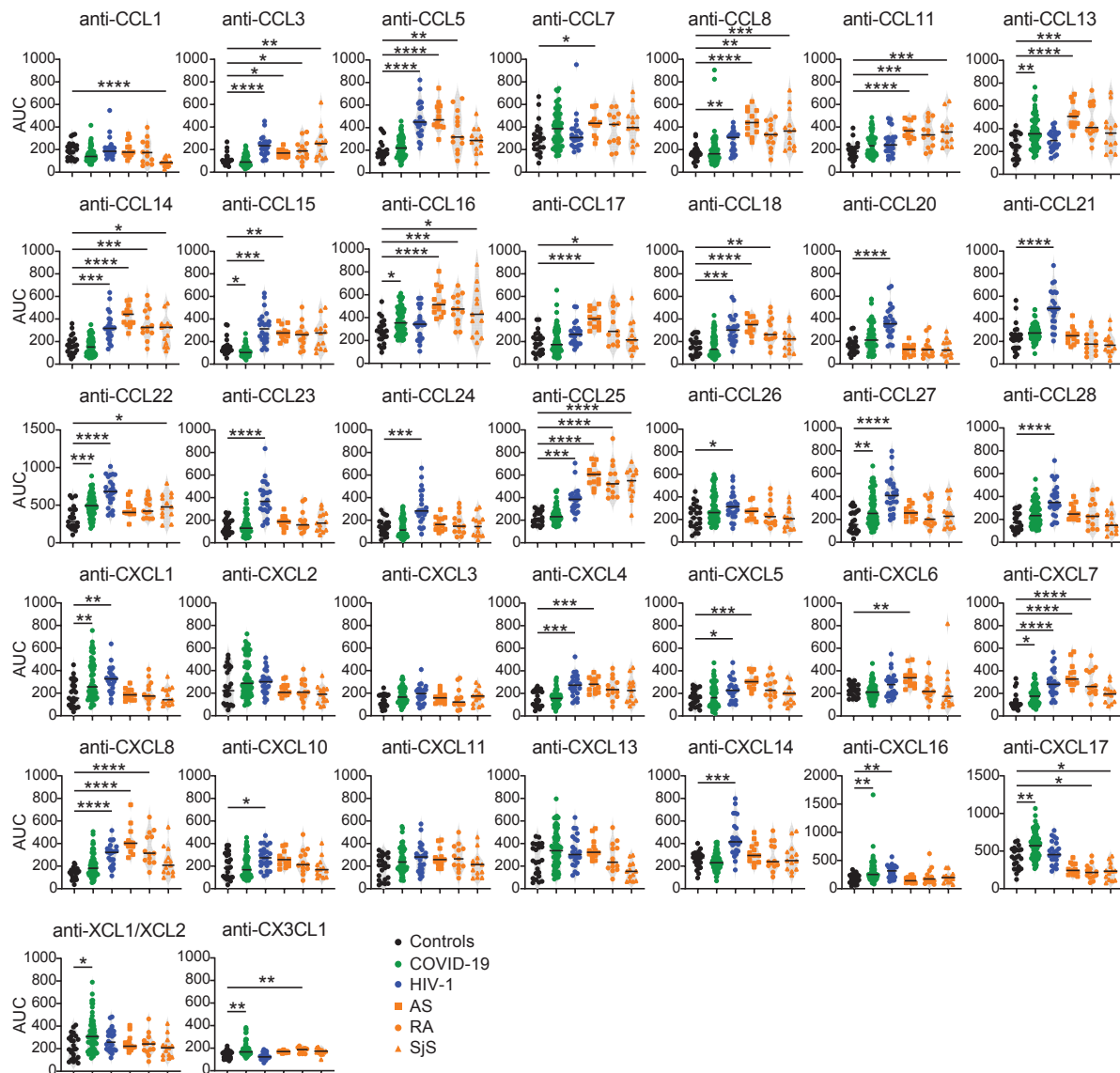
Figure S9

Fig. S9. Anti-chemokine N-loop antibodies in HIV-1 and autoimmune diseases, related to Fig. 4. The amount of plasma IgG antibodies against each chemokine N-loop was determined by ELISA for HIV-1 infected (n=24, blue) and autoimmune patients (n=39, orange). Autoimmune patients were subdivided in Ankylosing Spondylitis (AS, n=13), Rheumatoid Arthritis (RA, n=13), and Sjögren's syndrome (SjS, n=13). Values from controls (n=23, black), and COVID-19 convalescents (n=71, green) are shown alongside. Average AUC of two independent experiments. Horizontal bars indicate median values. Statistical significance was determined using Kruskal-Wallis test followed by Dunn's multiple comparison test over rank of the control group.
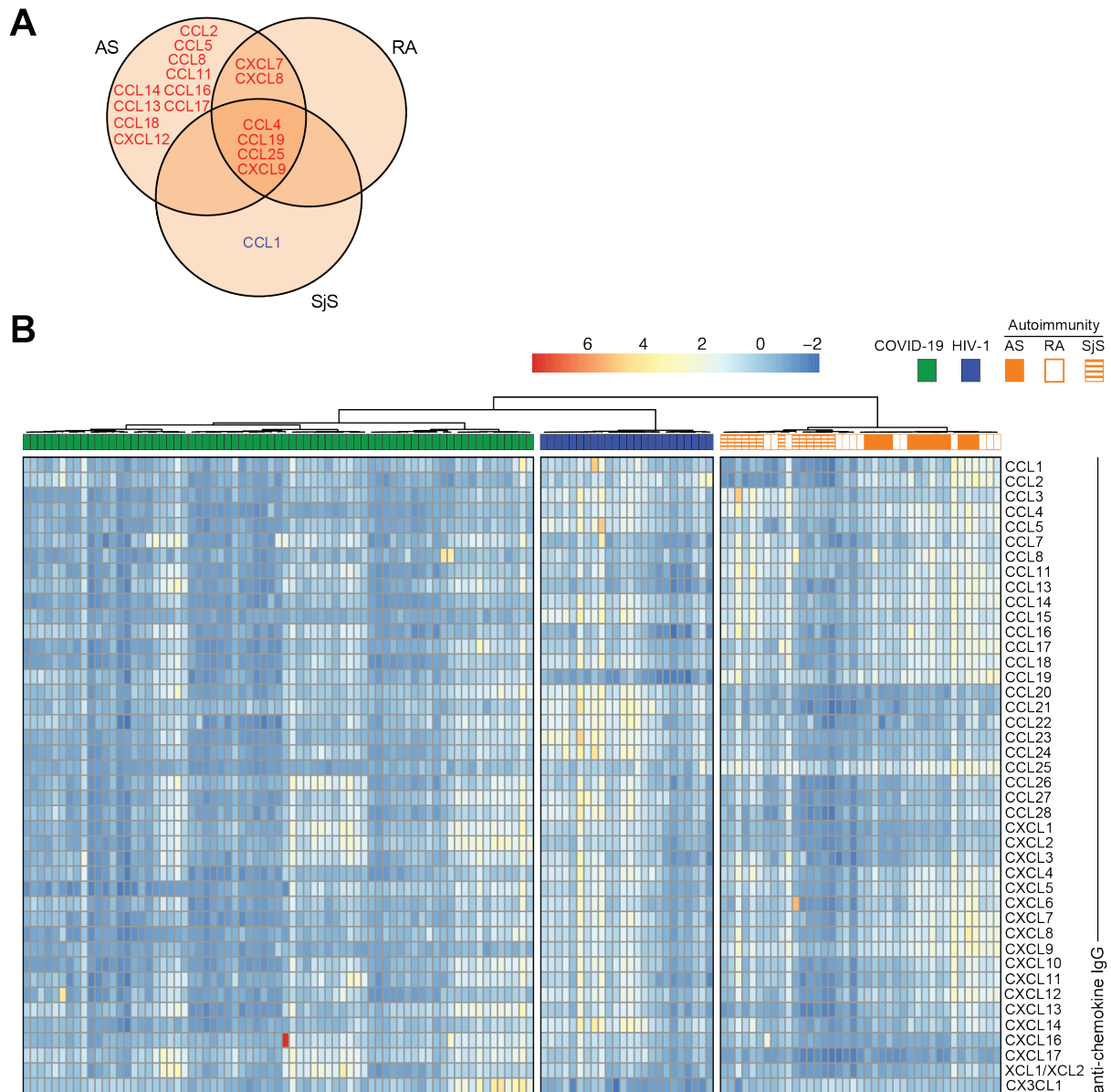
Figure S10

Fig. S10. Clustering of COVID-19, HIV-1 and autoimmune diseases based on anti-chemokine antibodies, related to Fig. 4. (**A**) Venn diagram of the chemokines targeted by autoantibodies across the autoimmune disorders AS, RA and SjS. Red and blue colors indicate either an increase or decrease over controls with $p<10^{-4}$. (**B**) Anti-chemokine antibodies correctly classify COVID-19 convalescents, HIV-1-infected, and patients with autoimmune disorders. Heatmap representing the normalized plasma IgG binding to 42 peptides comprising the N-loop sequence of all 43 human chemokines. Unsupervised hierarchical clustering analysis. The distribution of the groups within each cluster is shown.